日本磁気学会
ISSN 2432-0250
Journal of the Magnetics Society of Japan
Electronic Journal URL: https://www.jstage.jst.go.jp/browse/msjmag

Vol.50 No.2 2026

Journal

Magnetic Recording

Circularly Polarized Light-Induced Magnetization Reversal in Bi,Ga-Substituted Magnetic Garnet Films

R. Asatani, S. Suzuki, A. Hata, M. A. A. Masud, H. Sakaguchi, S. Isogami, and T. Ishibashi …30

Spintronics

Field-independent Superconducting Diode Effect and Field-Dependent Rectification Effect in Iron-Based Superconductors

U. Nagata, M. Aoki, A. Daido, S. Kasahara, Y. Kasahara, R. Ohshima, Y. Ando, Y. Yanase, Y. Matsuda, and M. Shiraishi …34

A Concept and Preparation of Disilicide Slurry for a Possible Detection of Chirality–Induced Spin Transport

K. M. Usama, Y. Kousaka, H. Shishido, and Y. Togawa …39

Structural Symmetry and Magnetoresistance in Epitaxial Fe/Ru/Co Multilayers

Y. Suzuki, T. Hattori, K. Hayashi, S. Iihama, and T. Moriyama …43

Power Magnetics

Performance Comparison of Interior Permanent Magnet Synchronous Motors with Amorphous Alloy and Silicon Steel Stator Core

I. Çirozlar, K. Nakamura …47

Study on Electromagnetic Force and Axial Uniformity of Electromagnetic Forming of 2024-Aluminum Alloy Tube Based on Double Magnetic Field Converter

C. Zerui, C. Jianghong, A. A-SIADA, L. Mengyao, Z. Jinrong, and C. Cheng …52

JOURNAL OF THE MAGNETICS SOCIETY OF JAPAN

Vol.50 No.2 2026

日本磁気学会

ISSN 2432-0250

HP: http://www.magnetics.jp/ e-mail: msj@bj.wakwak.com

Electronic Journal: http://www.jstage.jst.go.jp/browse/msjmag

TOEI

TPM-2-08s25

HcJの3σ/Ave. 0.2%※1を実現

渦電流補正方法※2も確立済

試料測定磁界
max 15Tesla

最大試料直径
10mm

パルス励磁型磁気特性測定装置

永久磁石および磁性体粉末を固形化した高磁化試料のヒステリシス曲線の自動測定および描画、SPD（Singuler Point Detection）測定が可能です。（RT～+200℃）

※1　電気学会資料 MAG-18-088 参照

※2　電気学会資料 MAG-07-011 参照

NdFeB(sintered) 測定例

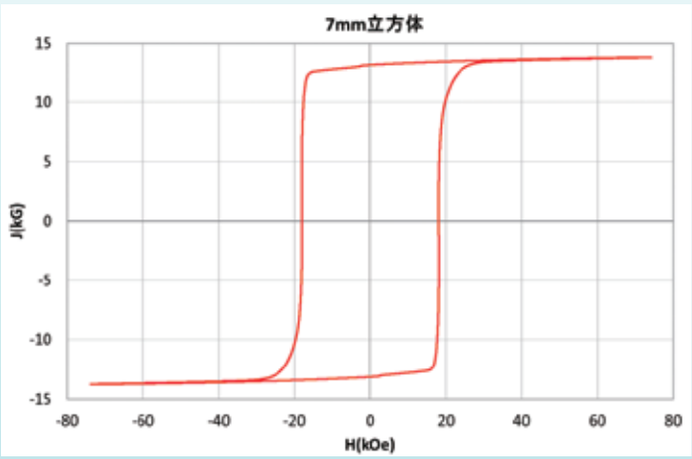

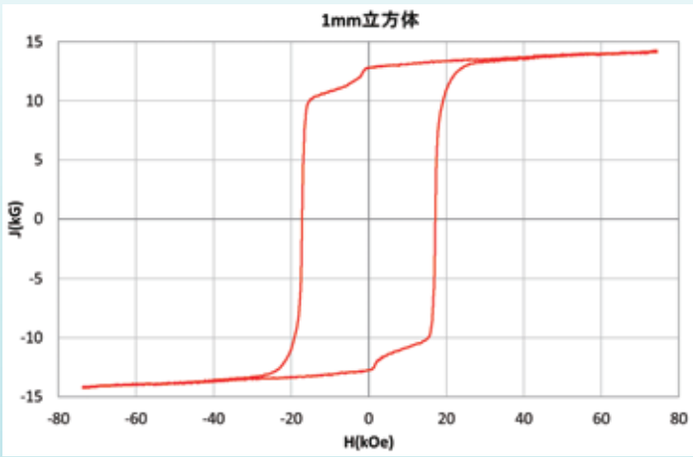

1mm 立方体測定用検出コイルはオプション品です

東英工業では他に振動試料型磁力計(VSM)、直流自記磁束計(JIS C2501 準拠)を始め、

各種磁気測定装置を取り揃えております。ぜひお問い合わせ下さい

TOEI 東英工業株式会社
http://www.toeikogyo.co.jp

〒194-0035 東京都町田市忠生1-8-13
TEL：042-791-1211 FAX：042-792-0490
E-mail：sales@toeikogyo.co.jp

Journal of the Magnetics Society of Japan
Vol. 50, No. 2

Electronic Journal URL: https://www.jstage.jst.go.jp/browse/msjmag

CONTENTS

Magnetic Recording

Circularly Polarized Light-Induced Magnetization Reversal in Bi,Ga-Substituted Magnetic Garnet Films
..... R. Asatani, S. Suzuki, A. Hata, M. A. A. Masud, H. Sakaguchi, S. Isogami, and T. Ishibashi 30

Spintronics

Field-independent Superconducting Diode Effect and Field-Dependent Rectification Effect in Iron-Based Superconductors
..... U. Nagata, M. Aoki, A. Daido, S. Kasahara, Y. Kasahara, R. Ohshima, Y. Ando, Y. Yanase, Y. Matsuda, and M. Shiraishi 34

A Concept and Preparation of Disilicide Slurry for a Possible Detection of Chirality–Induced Spin Transport
..... K. M. Usama, Y. Kousaka, H. Shishido, and Y. Togawa 39

Structural Symmetry and Magnetoresistance in Epitaxial Fe/Ru/Co Multilayers
Y. Suzuki, T. Hattori, K. Hayashi, S. Iihama, and T. Moriyama 43

Power Magnetics

Performance Comparison of Interior Permanent Magnet Synchronous Motors with Amorphous Alloy and Silicon Steel Stator Core
..... I. Çirozlar, K. Nakamura 47

Study on Electromagnetic Force and Axial Uniformity of Electromagnetic Forming of 2024-Aluminum Alloy Tube Based on Double Magnetic Field Converter
.....C. Zerui, C. Jianghong, A. A-SIADA, L. Mengyao, Z. Jinrong, and C. Cheng 52

J. Magn. Soc. Jpn., **50**, 30-33 (2026) <Letter>

Circularly Polarized Light-Induced Magnetization Reversal in Bi,Ga-Substituted Magnetic Garnet Films

R. Asatani, S. Suzuki, A. Hata, M. A. A. Masud, H. Sakaguchi, S. Isogami* and T. Ishibashi

Depart. Mater. Sci. and Bioeng., Nagaoka University of Technology, *1603-1 Kamitomioka, Nagaoka, Niigata 940-2188, Japan*

* Research Center for Magnetic and Spintronic Materials, National Institute for Materials Science, *1-2-1 Sengen, Tsukuba, Ibaraki 305-0047, Japan*

All-optical magnetization switching (AOS) in magneto-optical materials is promising phenomena for applications such as high-speed optical modulation technology, as it allows for magnetization reversal using only ultrashort laser pulses. We report on AOS induced by circularly polarized light in Bi,Ga-substituted magnetic garnet, $Bi_{2.5}R_{0.5}Fe_4GaO_{12}$ (R = Eu, Nd and Y), thin films prepared by the metal-organic decomposition method, which possess both large Faraday effect and perpendicular magnetic anisotropy. The experiments for circularly polarized light-induced magnetization reversal were performed using laser pulses with a wavelength of 514 nm and a pulse width of 230 fs. Helicity-dependent ring-shaped magnetic domains were formed around demagnetized domains for all samples, when approximately 200 pulses were cumulatively irradiated onto a single spot on the samples.

Keywords: magnetic garnet, ferrimagnetic materials, perpendicular magnetization, magneto-optical effect, circularly polarized light-induced magnetization reversal

1. Introduction

The advent of femtosecond pulsed lasers enabled the investigation of magnetization dynamics on timescales below 1 ps[1]. Subsequently, the phenomenon of All-optical magnetization switching (AOS) was discovered in Gd-Fe-Co thin films, where the magnetization reverses solely by the irradiation of a single laser pulse[2]. AOS is classified into helicity-independent AOS (HI-AOS) and helicity-dependent AOS (HD-AOS). Switching that is achieved with a single pulse is termed deterministic (or single-shot), while that which requires multiple pulses is referred to as cumulative (or multi-shot).

To date, deterministic HI-AOS has been reported in Gd-Fe-Co thin films[3] and Co-substituted Yttrium Iron Garnet (Co:YIG)[4]. Additionally, cumulative HI-AOS has been reported in materials such as $NiCo_2O_4$[5]. HI-AOS is a thermally driven process that has been reported to arise from differences in the demagnetization times of the spin sublattices of antiparallel aligned magnetic moments[6]. Consequently, HI-AOS has been considered a phenomenon unique to ferrimagnetic materials.

In contrast, deterministic HD-AOS has only been reported in Gd-Fe-Co thin films to date[2,3]. Other ferrimagnetic materials[7] and ferromagnetic materials, such as Co/Pt multilayer films[8], exhibited cumulative HD-AOS. The mechanism of HD-AOS was initially attributed to the inverse Faraday effect (IFE)[9]. However, subsequent studies suggested that the magnetic circular dichroism (MCD) effect during light absorption[10),11] in magnetic materials played a more dominant role.

Corresponding author: T. Ishibashi (e-mail: t_bashi@mst.nagaokaut.ac.jp).

Bi-substituted magnetic garnets examined in this study are ferrimagnetic materials that exhibit large magneto-optical (MO) effects. Given these features, it is highly plausible that HD-AOS could be observed in Bi-substituted magnetic garnets, which possess large MO effects. However, no AOS reports concerning Bi-substituted magnetic garnets have been published to date. Therefore, in this study, we investigated circularly polarized light-induced magnetization reversal using Bi- and Ga-substituted magnetic garnet films, $Bi_{2.5}R_{0.5}Fe_4GaO_{12}$ ($Bi_{2.5}Ga_1$:RIG) where R is rare-earth element, which possess excellent MO properties and perpendicular magnetic anisotropy (PMA). In this paper, we report on circularly polarized light-induced magnetization reversal in $Bi_{2.5}Ga_1$: RIG (R= Eu, Nd and Y) upon cumulative irradiation with laser pulses of varying polarization states.

2. Bi,Ga-substituted rare-earth iron garnet

Rare-earth iron garnets, $R_3Fe_5O_{12}$ (RIG) have a garnet crystal structure, in which iron ions, Fe^{3+}, occupy the tetrahedral and octahedral lattice sites, and rare-earth ions, R^{3+}, occupy the dodecahedral sites[12]. Within the molecular formula unit RIG, Fe^{3+} occupies three tetrahedral sites and two octahedral sites. Due to the antiferromagnetic coupling between these sites, the net magnetic moment per molecule $|\ 3 \times 5\ \mu_B - 2 \times 5\ \mu_B\ | = 5\ \mu_B$ [12]. On the other hand, the magnetic moments of the rare-earth ions vary depending on the specific rare-earth element.

It is well known that substituting Bi^{3+} for R^{3+} significantly enhances the MO effect[12]. Furthermore, Ga^{3+} substitution enables to reduce the saturation magnetization, since it has no magnetic moment and 90%

of the substituting Ga^{3+} replaces Fe^{3+} in the tetrahedral sites, resulting in a reduction of the demagnetization field ($4\pi M_S$)[13),14)]. In this study, Bi substitution amount was set to 2.5 to achieve a large Faraday rotation angle. In addition, to achieve PMA, the Ga substitution amount was set to 1.0 to decrease demagnetization filed[14)], and $Gd_3Ga_5O_{12}$ (GGG) single-crystal substrate with a (111) orientation was chosen to utilize that RIGs have the easy-axis of magnetization along the ⟨111⟩. Furthermore, to investigate the rare-earth ion dependence of the AOS induced by circularly polarized light, Eu, Nd and Y were selected as the rare-earth elements, where magnetic moments of Eu^{3+}, Nd^{3+} and Y^{3+} are oriented antiparallel, parallel, and exhibit no moment, respectively, with respect to the net magnetic moment of Fe^{3+} in the garnet structure[12)-16)].

$Bi_{2.5}Ga_1$:RIG (R = Eu, Nd and Y), i.e. $Bi_{2.5}Ga_1$:EIG, $Bi_{2.5}Ga_1$:NIG and $Bi_{2.5}Ga_1$:YIG, thin films were prepared on GGG (111) substrates using the MOD method[12)]. The MOD solutions, produced by Kojundo Chemical Laboratory Co., Ltd. were used. $Bi_{2.5}Ga_1$:EIG thin film was prepared using MOD solution prepared by mixing the MOD solutions, BiEuFe-04(2.5/0.5/5) and BiEuFeGa-04(2.5/0.5/3/2), in a 1:1 ratio. $Bi_{2.5}Ga_1$:NIG and $Bi_{2.5}Ga_1$:YIG thin films were prepared using BiNdFeGa-04 (2.5/0.5/4/1) and BiYFeGa-04 (2.5/0.5/4/1), respectively. For the MOD method, the GGG (111) substrate was placed in a spin coater, coated with the MOD solution, and spun at 3000 rpm for 30 s. This was followed by a drying process on a hot plate at 100℃ for 10 min, and then a pre-annealing at 450℃ for 10 min. In this study, the coating to pre-annealing process was repeated five times, followed by a final annealing at 700℃ for 3 h in an electric furnace. The total film thickness fabricated by this process is estimated to be approximately 150 nm.

The crystallinity of prepared $Bi_{2.5}Ga_1$:RIG thin films was characterized by the X-ray diffractometer (XRD) (Rigaku, SmartLab) using CuKα$_1$ radiation (λ = 0.154059 nm) for out-of-plane measurements monochromized with a double Ge (220) monochromator. Faraday rotation and ellipticity spectra and Faraday rotation hysteresis were measured using MO spectrometer, and magnetic domain structures were measured using MO imaging technique.

Figure 1 shows XRD patterns ($2\theta/\omega$ scan) of $Bi_{2.5}Ga_1$:EIG, $Bi_{2.5}Ga_1$:NIG and $Bi_{2.5}Ga_1$:YIG thin films, where an inset shows ϕ scan for (422) of $Bi_{2.5}Ga_1$:NIG. Diffraction peaks were clearly observed in the lower angle side of GGG 444 peak for all samples, which can be estimated as 444 diffraction peaks of $Bi_{2.5}Ga_1$:EIG, $Bi_{2.5}Ga_1$:NIG and $Bi_{2.5}Ga_1$:YIG thin films, respectively. The ϕ scan of the $Bi_{2.5}Ga_1$:NIG showed 6-fold symmetry,

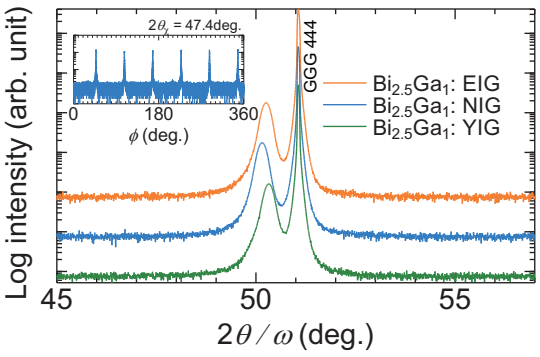

Fig. 1 X-ray diffraction patterns of $Bi_{2.5}Ga_1$:EIG, $Bi_{2.5}Ga_1$:NIG and $Bi_{2.5}Ga_1$:YIG thin films.

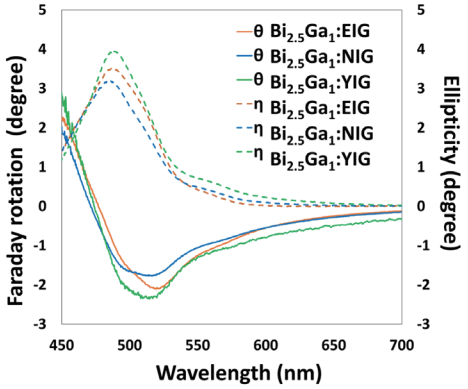

Fig. 2 Faraday rotation (solid line) and Ellipticity (dotted line) spectra of $Bi_{2.5}Ga_1$:EIG, $Bi_{2.5}Ga_1$:NIG and $Bi_{2.5}Ga_1$:YIG thin films.

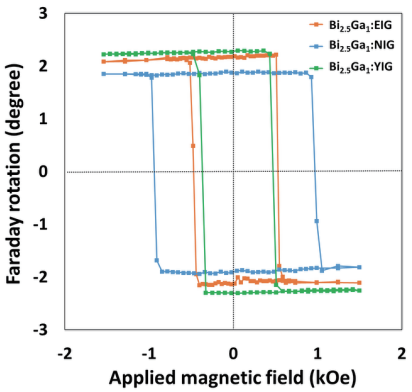

Fig. 3 Faraday rotation hysteresis of $Bi_{2.5}Ga_1$:EIG, $Bi_{2.5}Ga_1$:NIG and $Bi_{2.5}Ga_1$:YIG thin films.

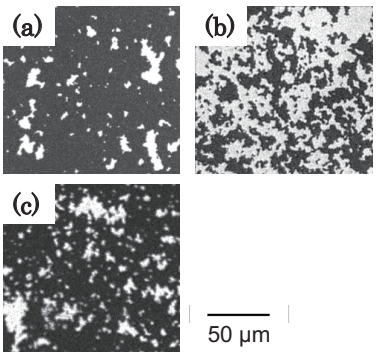

Fig. 4 MO images measured for demagnetized states of (a) $Bi_{2.5}Ga_1$:EIG, (b) $Bi_{2.5}Ga_1$:NIG and (c) $Bi_{2.5}Ga_1$:YIG thin films.

and similar results were obtained for the other two samples, not shown here. These results suggested that all samples were epitaxially grown with (111) orientation on GGG substrates. The out-of-plane lattice constants for the $Bi_{2.5}Ga_1$:EIG, $Bi_{2.5}Ga_1$:NIG and $Bi_{2.5}Ga_1$:YIG thin films were obtained to be 1.258, 1.260 and 1.255 nm, respectively.

Figure 2 shows Faraday rotation and ellipticity spectra of all samples, exhibiting the characteristic spectral shape of Bi-substituted rare-earth iron garnets. Faraday rotation and ellipticity angles at a wavelength of 514 nm were approximately -2° and 2°, respectively. Figure 3 shows Faraday rotation hysteresis of $Bi_{2.5}Ga_1$:EIG (at l = 519 nm), $Bi_{2.5}Ga_1$:NIG (at l = 514 nm) and $Bi_{2.5}Ga_1$:YIG (at l = 514 nm) thin films. The magnetic hysteresis loops showed a square shape, although the coercivity field (H_C) varied among the samples. These results suggested that the magnetic and MO characteristics in $Bi_{2.5}Ga_1$:RIG do not significantly depend on the rare-earth element.

Figure 4 shows MO images of $Bi_{2.5}Ga_1$:EIG, $Bi_{2.5}Ga_1$:NIG and $Bi_{2.5}Ga_1$:YIG measured at demagnetization states. Magnetic domain patterns indicating perpendicular magnetization are clearly observed. Many magnetic domains measuring several tens of microns were observed in the $Bi_{2.5}Ga_1$:EIG thin film, and it was found that their size was larger than that of $Bi_{2.5}Ga_1$:NIG or $Bi_{2.5}Ga_1$:YIG.

3. AOS experiments

Figure 5 illustrates the optical setup used in this experiment, which integrates the laser excitation and magneto-optical Kerr microscopy systems. The irradiation was performed using a Yb: KGW laser operating at a wavelength of 514 nm, a pulse duration of 230 fs, and a repetition rate of 10 kHz. A polarizer and a quarter-wave plate (QWP) were used to control the polarization state of the laser beam. The polarization-controlled laser pulses were focused onto the sample using a 20× objective lens with a numerical aperture (NA) of 0.45. The sample was fixed onto a sample stage capable of movement along the x and y axes. Observation of the formed magnetic domains was performed using a green LED with a wavelength of 520 nm as the light source and a polarization camera[17].

Laser pulses were delivered using both cumulative and scanning irradiation methods. In cumulative irradiation, the number of pulses directed onto the same spot was controlled by a shutter. In scanning irradiation, the sample stage was moved at a constant speed of approximately 50 μm/s during laser exposure. These experiments were conducted at room temperature (RT) and in ambient air. Prior to laser irradiation, an external magnetic field was applied to the sample to achieve magnetic saturation (i.e., aligning the magnetization uniformly in one direction).

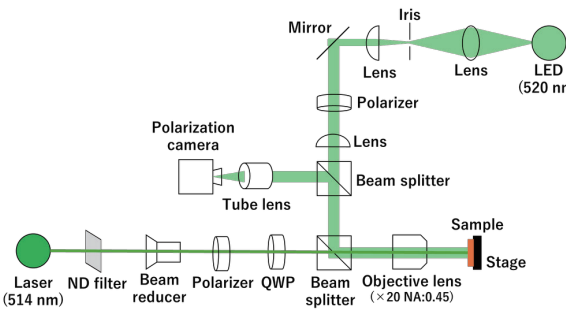

Fig. 5 Optical setup for AOS experiments.

Figure 6 shows the magnetic domain images of the $Bi_{2.5}Ga_1$:EIG, $Bi_{2.5}Ga_1$:NIG and $Bi_{2.5}Ga_1$:YIG film after cumulative irradiation with left-circularly polarized (LCP), linearly polarized (LP), and right-circularly polarized (RCP) light (from left to right) for both initial magnetization states, up (M+) and down (M–). The laser fluence for irradiation was set to 76 mJ/cm², and the number of accumulated pulses was 200.

As shown in Fig.6(a), when the initial magnetization was upward, cumulative irradiation with LCP and LP resulted in a demagnetized state, characterized by magnetic domains randomly oriented both upward and downward. Cumulative irradiation with RCP revealed the formation of an annular magnetization reversal domain (AOS ring), which is characteristic of cumulative HD-AOS, with a demagnetized state inside the ring. Conversely, when the initial magnetization was downward, LCP irradiation resulted in the formation of AOS ring with a central demagnetized state, while LP

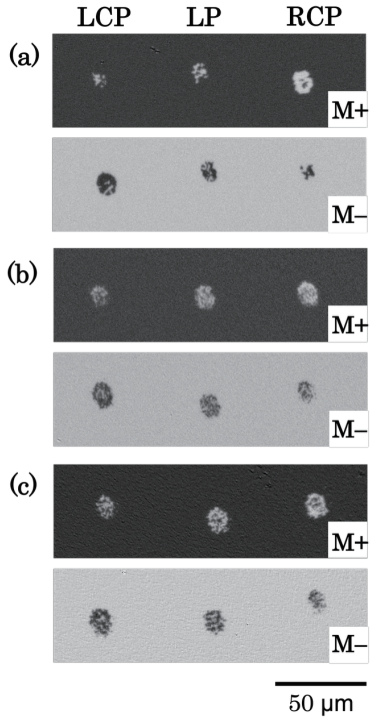

Fig. 6 MO images of (a) $Bi_{2.5}Ga_1$:EIG, (b) $Bi_{2.5}Ga_1$:NIG and (c) $Bi_{2.5}Ga_1$:YIG thin films. Initial magnetization direction: Black represents upward (M+), and white represents downward (M-).

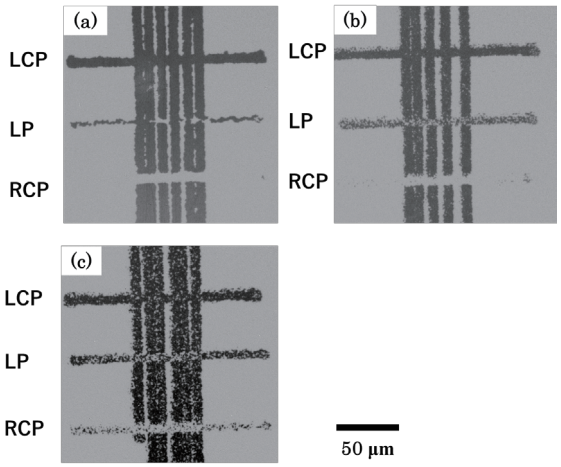

Fig. 7 MO images of (a) $Bi_{2.5}Ga_1$:EIG, (b) $Bi_{2.5}Ga_1$:NIG and (c) $Bi_{2.5}Ga_1$:YIG thin films measured after scanning irradiation with LCP, LP and RCP, where vertical line-shaped magnetic domains with opposite magnetization state M+ were written in advance by the scanning irradiation with LCP.

and RCP resulted only in a demagnetized state. Cumulative irradiation experiments were also conducted on $Bi_{2.5}Ga_1$:NIG and $Bi_{2.5}Ga_1$:YIG as shown in Figs. 6(b) and 6(c), respectively. In both samples, helicity-dependent AOS rings formed during the cumulative irradiation process as observed for the $Bi_{2.5}Ga_1$:EIG thin film.

Figure 7 shows MO images of the $Bi_{2.5}Ga_1$:EIG, $Bi_{2.5}Ga_1$:NIG and $Bi_{2.5}Ga_1$:YIG films measured after the scanning irradiation with LCP, LP and RCP with a laser fluence of 58 mJ/cm^2. Before the scanning with the three polarization states, the samples were magnetized in a downward magnetization state M–, and 5 or 6 vertical line-shaped magnetic domains with opposite magnetization state M+ were written by the scanning irradiation with LCP light at the same power. As shown in Fig. 7, regardless of the type of rare earth element in the samples, line-shaped magnetic domains with M+ and M– were obtained for LCP and RCP, respectively, and demagnetized domains were obtained for LP. These results clearly demonstrate HD-AOS in Bi-substituted rare-earth iron garnets, which is consistent with the results of other studies on HD-AOS[2,3,5,7,8]. The details of the rare earth dependence of HD-AOS will be reported in the near future.

Focusing on the MCD effect, which is considered crucial for the manifestation of HD-AOS, the $Bi_{2.5}Ga_1$:RIG film exhibits a large ellipticity angle. The ellipticity angle remains nearly constant even when the rare-earth ion is altered. Consequently, it is suggested that HD-AOS manifested similarly across the three $Bi_{2.5}Ga_1$: RIG samples. In other words, this high MCD effect is considered to play a major role in the manifestation of HD-AOS in Bi-substituted rare-earth iron garnets.

4. Conclusion

In conclusion, we demonstrated that the magnetization of $Bi_{2.5}Ga_1$:EIG, $Bi_{2.5}Ga_1$:NIG and $Bi_{2.5}Ga_1$:YIG thin films can be reversed by circularly polarized laser pulses without an external magnetic field, using a pulsed laser operating at a wavelength of 514 nm, a pulse duration of 230 fs, and a repetition rate of 10 kHz. This magnetization reversal is determined by the helicity of the circularly polarized light. We considered that high MCD effect of Bi,Ga-substituted magnetic garnets plays a major role in the manifestation of HD-AOS.

Acknowledgements This work was supported by NIMS Joint Research Hub Program, the Iketani Science and Technology Foundation, and joint research of the Institute of Materials and Systems for Sustainability of Nagoya University.

References

1) E. Beaurepaire, J.-C. Merle, A. Daunois, and J.-Y. Bigot: *Phys. Rev. Lett.*, **76**, 4250 (1996)
2) C. D. Stanciu, F. Hansteen, A. V. Kimel, A. Kirilyuk, A. Tsukamoto, A. Itoh and Th. Rasing: *Phys. Rev. Lett.*, **99**, 047601 (2007)
3) T. Ohkochi, R. Takahashi, H. Fujiwara, H. Takahashi, R. Adam, U. Parlak, K. Yamamoto, H. Osawa, M. Kotsugi, A. Tsukamoto, H. Wadati, A. Sekiyama, C. M. Schneider, M. Tsunoda, S. suga and T, Kinoshita: *J. Magn. Magn. Mat.*, **593**, 171854 (2024)
4) A. Stupakiewicz, K. Szerenos, D. Afanasiev, A. Kirilyuk, and A.V. Kimel: *Nature*, **542**, 71 (2017)
5) R. Takahashi, T. Ohkochi, D. Kan, Y. Shimakawa and H. Wadati: *ACS Appl. Electron. Mater.*, **5**, 748 (2023)
6) I. Radu, K. Vahaplar, C. Stamm, T. Kachel, N. Pontius, H. A. Dürr, T. A. Ostler, J. Barker, R. F. L. Evans, R.W. Chantrell, A. Tsukamoto, A. Itoh, A. Kirilyuk, Th. Rasing and A. V. Kimel: *Nature*, **472**, 205 (2011)
7) A. Ciuciulkaite, K. Mishra, M. V. Moro, I-A. Chioar, R. M. R-Robinson, S. Parchenko, A. Kleibert, B. Lindgren, G. Andersson, C. S. Davies, A. Kimel, M. Berritta, P. M. Oppeneer, A. Kirilyuk and V. Kapaklis: *Physical Review Materials*, **4**, 104418 (2020)
8) U. Parlak, R. Adam, D. E. Bürgler, S. Gang, and C. M. Schneider: *Phys. Rev. B.*, **98**, 214443 (2018)
9) T.D. Cornelissen, R. Cordoba and B. Koopmans: *Appl. Phys. Lett.*, **108**, 142405 (2016)
10) A.R. Khorsand, M. Savoini, A. Kirilyuk, A.V. Kimel, A. Tsukamoto, A. Itoh and Th. Rasing: *Phys. Rev. Lett.*, **108**, 127205 (2012)
11) J. Gorchon, Y. Yang and J. Bokor: *Phys. Rev. B*, **94**, 020409(R) (2016)
12) T. Ishibashi: *J. Magn. Soc. Jpn.*, **44**, 108 (2020)
13) G. Lou, T. Kato, S. Iwata and T. Ishibashi: *Optical Materials Express*, **7**, 2248 (2017)
14) M. Sasaki, G. Lou, Q. Liu, M. Ninomiya, T. Kato, s. Iwata and T. Ishibashi: *J. Appl. Phys.*, **55**, 055501 (2016)
15) M. A. A. Masud, W. Asano, K. Watanabe, M. Kawahara, F. Z. Chafi, M. Nishikawa, and T. Ishibashi, *IEEE Trans. Magn.*, **61**, 1 (2025)
16) R. Pauthenet: *J. Appl. Phys.*, **29**, 253 (1958)
17) H. Sakaguchi, R. Oya, S. Wada, T. Matsumura, H, Saito and T. Ishibashi: *J. Magn. Soc. Jpn.*, **46**, 37 (2022)

Received Oct. 21, 2025; Accepted Jan. 9, 2026

J. Magn. Soc. Jpn., **50**, 34-38 (2026) <Paper>

Field-independent Superconducting Diode Effect and Field-dependent Rectification Effect in Iron-based Superconductors

Utane Nagata[1], Motomi Aoki[1,2], Akito Daido[3], Shigeru Kasahara[4], Yuichi Kasahara[3], Ryo Ohshima[1,2], Yuichiro Ando[1,2], Youichi Yanase[2,3], Yuji Matsuda[3] and Masashi Shiraishi[1,2]

[1]Department of Electronic Science and Engineering, Kyoto University, *Kyoto, Kyoto 615-8510, Japan*

[2]Center for Spintronics Research Network, Institute for Chemical Research, Kyoto University, *Uji, Kyoto 611-0011, Japan*

[3]Department of Physics, Graduate School of Science, Kyoto University, *Kyoto 606-8502, Japan*

[4]Research Institute for Interdisciplinary Science, Okayama University, *Okayama, 700-8530, Japan*

The superconducting diode effect (SDE), where zero resistivity is realized in one current flow direction whereas non-zero resistivity in the opposite direction, is gathering tremendous fascination in both fundamental and applied physics because the SDE is a novel phenomenon resulting from symmetry breaking and enables the creation of low-power and low-noise electric circuit. Recently, a field-free SDE originating from a thermoelectric effect was reported in iron-based superconductors with nonmagnetic electrodes[1)]. Since amount of the research of the field-free SDE is very limited despite its importance in the perspective of symmetry breaking and possible realization of compact superconducting circuit without magnetic field, further understandings of the physical properties about the thermoelectric SDE are desired. Here, we investigate the SDE where ferromagnetic electrodes are equipped with iron-based superconductors to study the response of the SDE in the combination of an external magnetic field and ferromagnetic electrodes. Whereas the field-free thermoelectric SDE is dominant in the devices, the field-dependent and non-linear rectification effect are superimposed. The possible origin of the rectification is superposition of the two types of effects originating from Rashba type spin-orbit interaction.

Keywords: superconductor, superconducting diode effect, thermoelectric effect, rectification effect, Rashba type spin-orbit interaction, layered materials

1. Introduction

Iron-based superconductors possess abundant physical properties. FeSe is a representative and mother material[2)]. Its upper critical magnetic field is very large[3)], and recent studies revealed that FeSe is an extended s-wave superconductor[4)]. Its superconducting state is in the cross-over regime between weakly coupled Bardeen-Cooper-Schrieffer (BCS) and strongly coupled Bose-Einstein-condensate (BEC)[5)]. $FeTe_xSe_{1-x}$ (FTS) is a material, in which a part of selenium in FeSe is substituted with tellurium (Te), and exhibits superconductivity as well. Since FTS has Dirac cone and spin degeneracy is lifted at the surface due to the large spin orbit interaction of Te, it is a promising candidate for a topological superconductor[6), 7)].

Recently, such iron-based superconductors are also gathering great attention as material platforms of superconducting diode effect (SDE)[1), 8), 9)], which is a phenomenon that the critical current differs depending on the current flow direction[10)]. Many studies are actively implemented to clarify background physics of SDE theoretically[11)-16)] and experimentally[17)-23)], and now general understanding is that SDEs can be observed when time-reversal symmetry is broken under a magnetic field or the magnetization of materials in systems with spatial inversion symmetry breaking.

Corresponding author:
M. Shiraishi (e-mail: shiraishi.masashi.4w@kyoto-u.ac.jp).

However, more recently, a SDE originating from thermoelectric effect is observed in FeSe without magnetic fields that break the time reversal symmetry[1)]. In a superconducting system with temperature gradient, thermoelectric effect generates thermal supercurrent, which changes the net electric supercurrents flowing to opposite directions each other, resulting in the SDE. Since this type of the SDE is novel and has limited amount of research, it is significant to investigate the effect from multiple angles to gain further understandings of its nature.

The previous research[1)] unveiled that the thermoelectric SDE in an iron-based superconductor, FeSe, with nonmagnetic electrodes is fundamentally immune to an external magnetic field. Meanwhile, response of the SDE to the combination of an external magnetic field and ferromagnetic electrodes has not been surveyed yet, whereas the heterointerface of a ferromagnet/superconductor can create novel interface properties because the spin-orbit interaction (SOI) of ferromagnet cannot be neglected.

In this study, we investigate the response of the thermoelectric SDE in iron-based superconductors when ferromagnetic electrodes were equipped. The thermoelectric SDE, which is a field-free effect, remains dominant even in this case. Furthermore, we found that a magnetic-field-dependent and non-linear rectification effect is superimposed on the SDE. This rectification effect can be the consequence of the simultaneous occurrence of two phenomena at the interface of

superconductor and ferromagnetic electrodes, i.e., the vortex-induced rectification effect and nonreciprocal transport induced by magnetic field, which are due to the Rashba type spin-orbit interaction.

2. Detection of field-free SDE in FeSe with ferromagnetic electrodes

Figure 1(a) shows an optical image and measurement setup of a FeSe device with ferromagnetic Co electrodes. The FeSe was exfoliated and transferred onto a thermally oxidized Si substrate. The thickness of the FeSe flake was approximately 73 nm. Co (30 nm) / Au (80 nm) electrodes and pads were fabricated on the FeSe flake by using electron-beam (EB) lithography and EB deposition following to Ar^+ ion milling in a loadlock chamber. Mid-point-temperature of superconducting transition of the FeSe was measured to be 12 K. All of subsequent measurements were conducted in a physical property measurement system (PPMS; Quantum Design).

Figure 1(b) shows the I-V characteristics of the FeSe device as a function of temperature without an external magnetic field. Shifts in the critical current $\Delta I_c = I_{c+} - I_{c-}$ were clearly observed below 10 K, i.e., the field-free SDE was successfully observed in the FeSe device with ferromagnetic electrodes. ΔI_c increased as the temperature decreased and the diode efficiency $\eta = \Delta I_c / (I_{c+} + I_{c-})$ reached 11 % at 5 K, which are the same tendency and comparable to the thermoelectric SDE observed in FeSe with nonmagnetic electrodes in the previous study[1]. This finding signifies that the SDE attributed to the thermoelectric effect is still dominant when ferromagnetic electrodes are attached.

To support the existence of the field-free SDE, the measurement using an AC electric current, I_{AC}, is conducted. The frequency of I_{AC} is set to be 17 Hz and its 0-peak amplitude (not the root mean square value) was swept from 0 mA to 3 mA without an external magnetic field. Then, the AC voltages were measured by lock-in amplifiers as a root-mean-square value. Figure 1(c) shows the I_{AC} dependence of the first harmonic voltages ($V\omega$). The value of $V\omega$ is finite due to the transition from the superconducting to the normal state when the amplitude of the AC current becomes larger than the critical current. Figure 1(d) shows the I_{AC} dependence of the second harmonic voltages ($V_2\omega$). Salient peaks in $V_2\omega$ are observed at an I_{AC} of the critical current at 5 and 6 K, where the sharp increase in $V\omega$ occurs. Given that the $V_2\omega$ is attributed to the rectification effect, the amplification of $V_2\omega$ at the critical current buttresses the

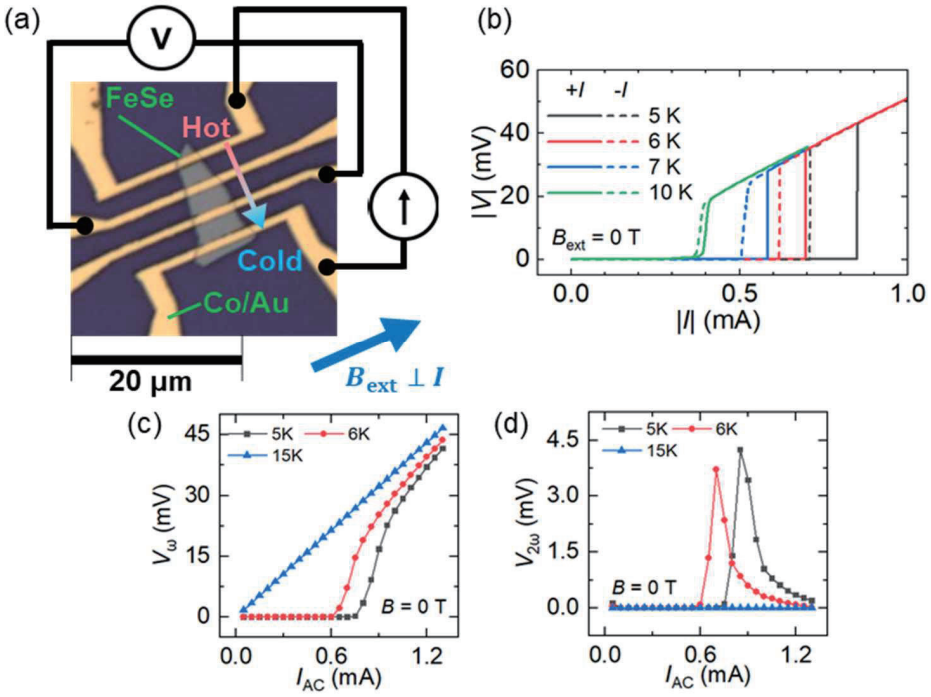

Fig. 1. (a) Measurement setup and the fabricated FeSe device image. A blue arrow shows the direction of the applied external magnetic field. A red and blue gradation arrow shows temperature gradient in the FeSe device. (b) I-V characteristics of the device at from 5 to 10 K under positive (the solid lines) and negative (the dashed lines) electric currents. The black, red, blue, and green lines show the I-V curves at 5, 6, 7, and 10 K, respectively. An external magnetic field was not applied. (c) AC current dependence of first-harmonic voltage at from 5 to 15 K. (d) AC current dependence of second-harmonic voltage at from 5 to 15 K. The black, red, and blue lines show the I_{AC}-V_ω curves at 5, 6, and 15 K, respectively. The frequency of the applied current was set to be 17 Hz. An external magnetic field was not applied in the measurements shown in this figure, but it was applied in the measurement shown in Section 4.

successful observation of the difference in I_{c+} and I_{c-}. In addition, the magnitude of the peak of the $V_{2\omega}$ gradually and monotonically decreased as the temperature increased up to T_c and approached to zero at 15 K, where the FeSe transitioned to the normal conducting state. This finding is consistent with the monotonic decrease in ΔI_c with increasing temperature, as shown in Fig. 1(b). Moreover, this temperature dependence of $V_{2\omega}$ is also consistent with the feature of thermoelectric SDE with nonmagnetic electrodes[1]. This result supports the validity of our assertion of the successful detection of the field-free SDE originated from thermoelectric effect in FeSe with ferromagnetic electrodes.

3. SDE in $FeTe_{0.6}Se_{0.4}$ with ferromagnetic electrodes

We also investigated the response of the field-free SDE in $FeTe_{0.6}Se_{0.4}$ (FTS) device with ferromagnetic Co electrodes. To note is that since the Seebeck coefficient of FTS is comparable to that of FeSe[24, 25], FTS is also suitable for the investigation of properties of thermoelectric SDE despite the fact that representative material platform of the thermoelectric SDE is FeSe[1]. Furthermore, Te incorporation may tune intrinsic SOI in FTS compared to FeSe, which can provide a material to discuss the role of SOI in the following section.

Figure 2(a) shows an optical image and measurement setup of the FTS device with Co electrodes. FTS was exfoliated and transferred onto a thermally oxidized Si substrate. The thickness of the FTS flake was approximately 94 nm. Co (30 nm) / Au (70 nm) electrodes and pads were fabricated on the FTS flake by using EB lithography and EB deposition following to Ar^+ ion milling in a loadlock chamber. Mid-point-temperature of superconducting transition of the FTS was measured to be 14 K.

Figure 2(b) shows the I-V characteristics of the FTS device as a function of temperature without external magnetic field. The non-zero ΔI_c were clearly observed below 13 K, i.e., the field-free SDE was also successfully observed in the FTS device with ferromagnetic electrodes. ΔI_c increased as the temperature decreased and the diode efficiency $\eta = \Delta I_c / (I_{c+} + I_{c-})$ reached 0.93 %, which are the same tendency to the thermoelectric SDE observed in FeSe with nonmagnetic electrodes in the previous study[1].

To confirm a response to an external magnetic field, B_{ext}, the B_{ext} was applied to the device in-plane and perpendicular to the current flow direction. Figures 2(c)-(f) show the B_{ext} dependence of ΔI_c at 4 K, 7 K, 10 K and 13 K, respectively. ΔI_c is immune to B_{ext} at 4 K, 7 K, and 10 K like the thermoelectric SDE in FeSe[1]. The decrease of ΔI_c as B_{ext} increases at 13 K is due to that the superconductivity of FTS is almost broken by temperature and a high magnetic field. These results ensure that the SDE attributed to the thermoelectric effect is also dominantly observed in the FTS device with ferromagnetic electrodes.

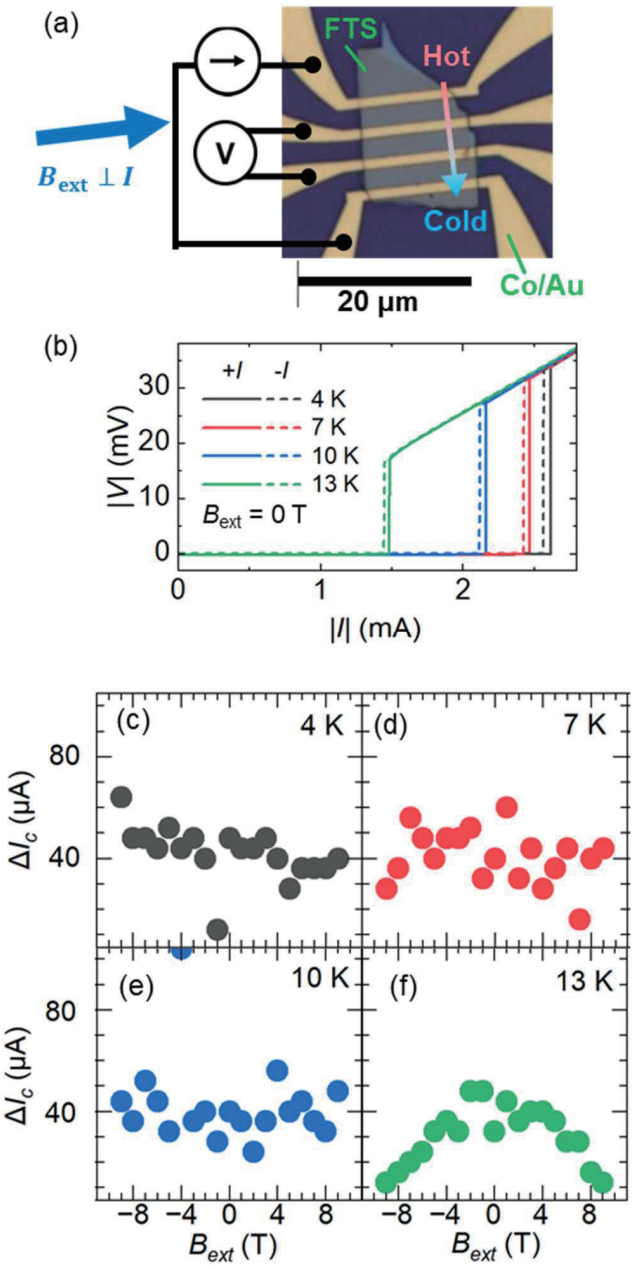

Fig. 2. (a) Measurement setup and the fabricated FTS device image. A blue arrow shows the direction of the applied external magnetic field. A red and blue gradation arrow shows temperature gradient in the FTS device. (b) I-V characteristics of the device at from 4 to 13 K under positive (the solid lines) and negative (the dashed lines) electric currents. The black, red, blue, and green lines show the I-V curves at 4, 7, 10, and 13 K, respectively. An external magnetic field was not applied. (c)-(f) External magnetic field dependence of ΔI_c at temperatures ranging from 4 to 13 K.

4. Field-dependent rectification effect in iron-based superconductors with ferromagnetic electrodes

Although thermoelectric effect is dominant at around the critical current of the FTS, a rectification effect originated from the interface between FTS and ferromagnetic electrodes is superimposed when the zero resistivity starts to break at around the critical current. To characterize the rectification effect quantitatively, we define a difference of a four-terminal voltage ΔV as $\Delta V = V(+I) - V(-I)$, where I is an electric current. Figure 3(a) shows current dependence of the ΔV of the device shown in Fig. 2(a) when the magnetic field of ±9 T is applied at 10 K. The direction of the magnetic field is the same as shown by the blue arrow in Fig. 2(a). Absolute value of ΔV gradually increases as absolute value of current increases below 1.7 mA, which indicates resistance of FTS differs depending on current flow direction when the current amplitude increases, i.e., a rectification effect is observed. More importantly, the polarity of ΔV below I = 1.7 mA is reversed when the magnetic field direction is reversed. Thus, this rectification effect is field-dependent. Large fluctuation in ΔV above 1.7 mA is most likely due to the difference of critical current originated from thermoelectric effect because polarity of the fluctuation is independent of the magnetic field. Figure 3(b) shows the magnetic field B_{ext} dependence of ΔV normalized by the applied current density $J_{FTS/Co}$ (= 1.3×10^9 A/m^2), where the absolute value of applied current is 1.5 mA at 10 K. We note that to discuss the role of interfacial spin-orbit interaction (SOI), ΔV is normalized by the applied current density. The normalized ΔV exhibits odd-function behavior to the magnetic field. The noteworthy is that $\Delta V/J_{FTS/Co}$ reaches the minimum/maximum value when B_{ext} = +3 and −3 T, and its sign changes when $|B_{ext}| > 5$ T.

The underlying physics of the field-dependent rectification effect is as follows: This effect can be ascribed to the superposition of two types of interface nature due to the Rashba type SOI between the Co and the FTS.

While FTS is a candidate material for a topological superconductor (TSC)[6), 7)] and TSC can host nonreciprocal transport[26)], this is not the origin of the rectification effect. Nonreciprocal transport in TSC should merely behave linearly to the magnetic field[26)], whereas the finding of the rectification effect in FTS is not. The existence of the rectification effect with the same B_{ext} dependence in the FeSe shown in fig. 1(a), which is not TSC but an extended s-wave superconductor[4)], also supports our assertion (see also Fig. 3(c)). The direction of the magnetic field in the FeSe device is shown by the blue arrow in Fig. 1(a).

The Rashba type SOI can generate vortex-induced rectification effect at an interface of a superconductor[8)], and the Rashba type SOI also allows nonreciprocal charge transport expressed as,

$$R = R_0 [1 + \gamma(\boldsymbol{B} \times \boldsymbol{P}) \cdot \boldsymbol{I}], \qquad (1)$$

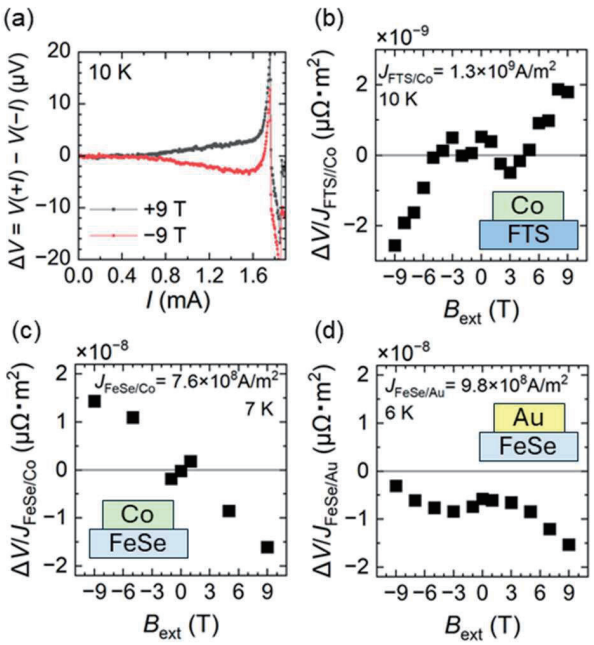

Fig. 3. (a) Applied current dependence of ΔV at 10 K. The black and red lines show ΔV when external magnetic field is +9 T and -9 T, respectively. The device is the same as that shown in Fig. 2 (a). (b) External magnetic field dependence of ΔV normalized by applied current density $J_{FTS/Co}$ (= 1.3×10^9 A/m^2) at 10 K in the FTS/Co device. Applied current value was 1.5 mA. (c) External magnetic field dependence of ΔV normalized by applied current density $J_{FeSe/Co}$ at 7 K, when absolute value of $J_{FeSe/Co}$ = 7.6×10^8 A/m^2 in the FeSe device with Co electrodes. The device is the same as that shown in Fig. 1 (a). The orientation of magnetic field is shown by a blue arrow in Fig. 1 (a). (d) External magnetic field dependence of ΔV normalized by applied current density $J_{FeSe/Au}$ at 6 K, when absolute value of $J_{FeSe/Au}$ = 9.8×10^8 A/m^2 in the FeSe device with Au electrodes.

where R is resistance, $\boldsymbol{P}$ is a direction of inversion symmetry breaking and γ is the coefficient of magnetochiral anisotropy[10), 27)].

As for the former effect, the Rashba type SOI forms asymmetric pinning potential in the superconductor parallel to the potential gradient ∇V of the Rashba type SOI, resulting in the rachet motion of vortices when an external magnetic field $\boldsymbol{B}$ is applied, which induces rectification effect of supercurrent perpendicular to both ∇V and $\boldsymbol{B}$[8)]. This rectification effect is enhanced as $\boldsymbol{B}$ increases, maximized at around 5 T and suppressed over 5 T in FTS/FeTe heterostructure while the reason of the suppression is still unclear[8)]. The asymmetric pinning potential can be emerged wherever a potential gradient exists. In our FTS device, a potential gradient exists along the out-of-plane direction to the device at the interface between FTS and Co electrodes, external magnetic field is applied along the in-plane direction to the device, and the current is applied perpendicular to

both the potential gradient and the magnetic field. Therefore, the vortex-induced rectification effect can appear in our device as in the case of ref. 8). The notable is that the influence of the potential gradient at the interface between the FTS top surface and the air can be canceled out by that of the potential gradient at the interface between the FTS bottom surface and the thermally oxidized silicon substrate, which is an insulator, because the direction of the potential gradient is opposite. Hence, it is signified that the phenomenon due to the net potential gradient can simply resulted from the interface between FTS and Co.

The nonreciprocity due to the latter effect is enhanced linearly as $\boldsymbol{B}$ increases as understood from Eq. (1). In our device, $\boldsymbol{P}$ is along the potential gradient of the interface between FTS and Co, i.e., along the out-of-plane direction to the device. The direction of the applied magnetic field, the electric current and the potential gradient are orthogonal to each other. Therefore, the $\boldsymbol{B}$-linear nonreciprocal transport can appear in our device as well.

When the two effects can coexist simultaneously in the FTS device, the vortex-induced rectification effect is dominant in the low-magnetic-field region and suppressed at high-magnetic-field region above 5 T. Instead, the $\boldsymbol{B}$-linear nonreciprocal transport becomes dominant at the high-magnetic-field region, which cancels out the vortex-induced effect and changes the sign of ΔV. Therefore, by postulating that the two effects originating from the interface of the FTS/Co can manifest themselves simultaneously, the sign reversal behavior of the rectification effect can be well explained.

A control experiment using an FeSe device with Au electrodes also supports the contribution of interfacial SOI to the non-linear rectification. As shown in Figure 3(d), the non-linear rectification is also observed in the FeSe/Au device, whereas the origin of negative offset is elusive. The amplitude of normalized ΔV in the FeSe/Au is smaller than the FeSe/Co devices although $J_{\mathrm{FeSe/Au}}$ is larger than $J_{\mathrm{FeSe/Co}}$. This result implies that the non-linear rectification effect is determined by interface of devices, i.e., the interfacial SOI can govern the ΔV.

The polarity reversal of ΔV between FTS and FeSe (see Figs. 3(b) and 3(c)) can be holistically understood by assuming the potential gradient of FTS/Co and FeSe/Co are in the opposite direction. This assertion is plausible because the large atomic number of Te in FTS can reverse the potential gradient compared with FeSe/Co. For further exploration of this rectification phenomenon, it is necessary to investigate the magnitude relationship of potential gradient between superconductors and materials of ferromagnetic or nonmagnetic electrodes systematically.

5. Conclusion

In summary, we investigated the thermoelectric SDE of iron-based superconductors with ferromagnetic electrodes, where the field-dependent and non-linear rectification effects are superimposed. The finding can be attributed to the combination of the vortex-induced rectification effect and the nonreciprocal transport by the Rashba type SOI at the interface between iron-based superconductors and ferromagnetic electrodes.

Acknowledgements This work is partly supported by the JSPS Grant-in-Aid for Challenging Research (No. 23K17353). U.N. would like to thank the Hirose Foundation for their financial support through a scholarship.

References

1) U. Nagata, et al.: *Phys. Rev. Lett.*, **134**, 236703 (2025).
2) F. -C. Hsu, et al.: *PNAS*, **105**, 14262 (2008).
3) S. I. Vedeneev, et al.: *Phys. Rev. B*, **87**, 134512 (2013).
4) J. -Y. Lin, et al.: *Phys. Rev. B*, **84**, 220507(R) (2011).
5) S. Kasahara, et al.: *PNAS*, **111**, 16309 (2014).
6) P. Zhang, et al.: *Science*, **360**, 182 (2018).
7) Y. -F. Li, et al.: *Phys. Rev. X*, **14**, 021043 (2024).
8) Y. Kobayashi, et al.: *Commun. Phys.*, **8**, 196 (2025).
9) G. Qiu, et al.: arXiv:2303.00966 (2023).
10) F. Ando, et al.: *Nature*, **584**, 373 (2020).
11) N. F. Q. Yuan and L. Fu: *PNAS*, **119**, e2119548119 (2022).
12) A. Daido, et al.: *Phys. Rev. Lett.*, **128**, 037001 (2022).
13) Y. Zhang, et al.: *Phys. Rev. X*, **12**, 041013 (2022).
14) S. Ilić and F. S. Bergeret: *Phys. Rev. Lett.*, **128**, 177001 (2022).
15) H. F. Legg, et al.: *Phys. Rev. B*, **106**, 104501 (2022).
16) J. J. He, et al.: *New J. Phys.*, **24**, 053014 (2022).
17) H. Narita, et al.: *Nat. Nanotechnol.*, **17**, 823 (2022).
18) C. Baumgartner, et al.: *Nat. Nanotechnol.*, **17**, 39 (2022).
19) Y. Hou, et al.: *Phys. Rev. Lett.*, **131**, 027001 (2023).
20) L. Bauriedl, et al.: *Nat. Commun.*, **13**, 4266 (2022).
21) B. Pal, et al.: *Nat. Phys.*, **18**, 1228 (2022).
22) A. Sundaresh, et al.: *Nat. Commun.*, **14**, 1628 (2023).
23) H. Wu, et al.: *Nature*, **604**, 653 (2022).
24) T. M. McQueen, et al.: *Phys. Rev. B*, **79**, 014522 (2008).
25) P. D. Lodhi, et al.: *J. Supercond. Nov. Magn.*, **31**, 2671 (2018).
26) M. Masuko, et al.: *nqj Quantum Mater.*, **7**, 104 (2022).
27) G. L. J. A. Rikken and P. Wyder: *Phys. Rev. Lett.*, **94**, 016601 (2005).

Received Oct. 01, 2025; Accepted Jan. 09, 2026

J. Magn. Soc. Jpn., **50**, 39-42 (2026) <Letter>

A concept and preparation of disilicide slurry for a possible detection of chirality–induced spin transport

Khan Muhammad Usama, Yusuke Kousaka, Hiroaki Shishido, and Yoshihiko Togawa
Department of Physics and Electronics, Osaka Metropolitan University, *Sakai, Osaka 599-8531, Japan*

A concept of chiral slurry for a possible detection of spin-charge interconversion phenomena is presented. Here slurry was made by mixing niobium disilicide $NbSi_2$ powders with additive conductive paste in an organic solvent. A systematic study has been performed to examine how the increase in the weight percentage of silver paste in the $NbSi_2$ slurry influences the electrical transport properties. It was found that the samples coated with the $NbSi_2$ slurry exhibited longitudinal and transverse voltage responses. Importantly, the transverse signal decreases monotonically as the silver weight percentage increases in the slurry. The obtained data support that the silver paste is useful as a conductive auxiliary for controlling the slurry resistivity and transverse voltage signals in printable devices. This work provides a preliminary and essential foundation for investigating the intrinsic chirality-induced spin selectivity effect in chirality-controlled powders in the future experiments.

Keywords: spin–charge interconversion, chirality, niobium disilicide, slurry, printed film

1. Introduction

Spintronics plays a vital role in utilizing the spin degree of electrons in various applications, such as storage devices and computing[1)-3)]. Spintronic devices offer several advantages over conventional devices, involving efficiency in data processing, non-volatile functionality, device integrity, and reduced power consumption. The primary challenge in spintronic devices is to generate and detect efficient spin currents[1)]. Generally speaking, spin–orbit coupling (SOC) is essential for the spin-charge interconversion. The SOC results in the emergence of various physical phenomena, including the spin hall effect (SHE)[4),5)] and the Rashba-Edelstein effect (REE)[6)]. In the SHE, the spin current diffuses perpendicularly to the orientations of spin and electric current due to the SOC, while in the REE, the electric current induces spin polarization in materials with broken inversion symmetry. In this connection, a lack of inversion symmetry in chiral materials makes them encouraging, where unconventional spin responses appear. Indeed, the spin-filtering effect, analogous to the REE, has been reported in chiral molecules solely composed of light elements with weak SOC[7)-10)].

Chiral inorganic crystals offer a promising platform for exploring the spin–charge interconversion as well. Their intrinsic structural asymmetry, when combined with the SOC, can enable spin-dependent transport phenomena without magnetic field[11)-13)]. In addition, the understanding of the spin-charge conversion process in polycrystalline powders remains a subject worthy of detailed investigation[14),15)]. The motivation to use polycrystalline powders remains limited because they are perceived as having structural disorder due to multiple grain boundaries, which may affect electronic uniformity. However, some inorganic polycrystalline powders could be available on a commercial scale and utilizing such powders may be advantageous for device applications. In a different point of view, slurry-based inorganic materials have become promising candidates for flexible electronics because they are easy to process, compatible with printing techniques and suitable for uniform coating on various substrates[16)-20)]. Their ability to be shaped and deposited into flexible forms makes them ideal for integration into stretchable, bendable, and wearable devices. To date, several flexible spintronics devices have been reported[21)-25)].

Here we come up with the idea of making a slurry of polycrystalline powders of the chiral material. It can help us investigate preliminary properties associated with the conventional spin-charge interconversion process and promote the development of cost-effective slurry-based devices. Typically, such devices are made using organic molecules, including chiral polymers[26),27)]. However, there are several advantages of inorganic chiral slurry over chiral polymers, such as mechanical adaptability, temperature stability and controllable electrical resistivity by varying the conductive content. These features may make an inorganic chiral slurry preferable for flexible platforms.

In this Letter, we present the slurry made from polycrystalline powders of $NbSi_2$, which is one of the representative chiral inorganic materials. In the fabricated devices, which are made of the powders with their chirality uncontrolled, our aim is not to detect chirality directly but to investigate a possible detection of the spin–charge interconversion by correlating the longitudinal voltage V_{xx} and transverse voltage V_{xy} and V_{yx} in $NbSi_2$ slurry samples at room temperature

Corresponding author:
K. M. Usama (e-mail: sx23488x@st.omu.ac.jp).

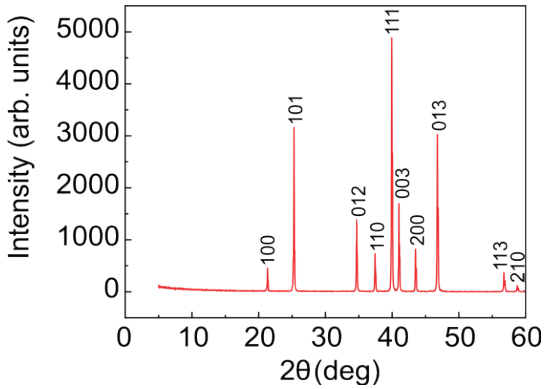

Fig. 1 X-ray diffraction pattern of $NbSi_2$ powders.

without a magnetic field. The emergence of transverse voltage signals in the local configuration would be a key element in determining the intrinsic chirality-induced spin selectivity (CISS) effect when chirality-controlled powders are used in future experiments.

2. Material and device preparations

The $NbSi_2$ compound exhibits a C40-type crystal structure and belongs to a space group $P6_222$ or $P6_422$, which respectively provides right-handed or left-handed chirality domains in polycrystalline powders and makes them scalemic or racemic in terms of chirality. The size of unit cell is 0.4798 nm along the *a*-axis and 0.6592 nm along the *c*-axis and no magnetic order appears [28),29)].

$NbSi_2$ powders were prepared by a solid-state reaction method. Niobium (-325 mesh, 99.9% purity, rare metallic Co. Ltd) and silicon (-100 mesh, 99.9% purity, rare metallic Co. Ltd.) commercial powders were used as the starting materials. A stoichiometric mixture of Nb and Si was heated at 1100°C in a vacuumed quartz tube for two days. X-ray diffraction (XRD) analysis revealed a single-phase pattern without any detectable impurities, indicating the high purity of the synthesized material, as shown in Fig. 1.

$NbSi_2$ powders used for fabricating the slurry were synthesized without a chiral seed. Thus, the prepared slurry consists of right and left chirality domains and exhibits an asymmetric crystal structure with a polycrystalline nature. In polycrystalline materials, it is not possible to determine the percentage of handedness (i.e., the ratio of left-handed and right-handed chiral domains) using conventional X-ray diffraction analysis.

For electrical transport measurements, the polycrystalline powders were utilized in a slurry form. The powders were first grinded into fine particles by a mortar and pestle for homogeneous slurry formation. Morphological analysis of the $NbSi_2$ powders was performed using scanning electron microscopy (SEM). Figure 2(a) shows the SEM image taken at a magnification of ten thousand with an operating voltage of 5.0 kV. The average particle size of the polycrystalline powders is around 1 μm. Then, the slurry was synthesized by mixing the milled $NbSi_2$ as an

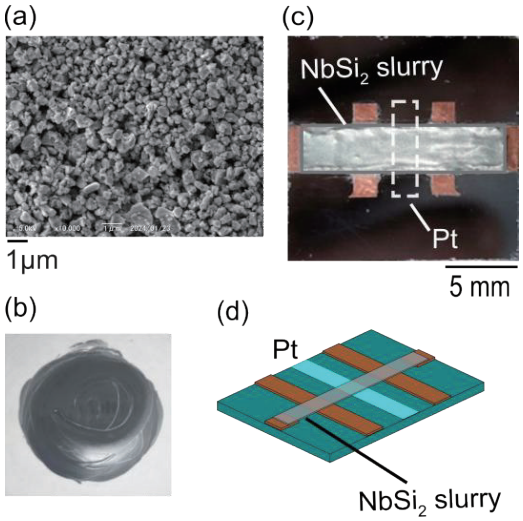

Fig. 2 A preparation of $NbSi_2$ slurry and printed device for a possible detection of the CISS response. A SEM micrograph of polycrystalline $NbSi_2$ powder (a), optical photographs of synthesized $NbSi_2$ slurry (b) and of the printed device made of $NbSi_2$ slurry (c) with a schematic drawing of the device structure (d).

active material, silver paste as an additive conductive element, and xylene as a dilute solution, as shown in Fig. 2(b). Five samples of $NbSi_2$ slurry were synthesized by varying the silver weight percentages at 5%, 8%, 10%, 20% and 30%.

The device was fabricated on a 20 × 20 mm^2 silicon substrate with four copper strips that are used as the electrodes for the current injection and V_{xx} detection. These copper strips were cut using a milling machine and bonded to the silicon substrate. For a possible detection of the inverse SHE response, a platinum (Pt) electrode of 2 mm in width and 14 nm in thickness was deposited at the center of the substrate through a metal mask via a magnetron sputter (MSP-1S, Vacuum Device, Inc.). The prepared slurry was then cast in a rectangular shape of 16 mm in length, 4 mm in width and 1 mm in thickness directly onto the silicon substrate using the printing technique, as illustrated in Fig. 2(c). Finally, the printed slurry samples were dried at room temperature.

All the electrical transport measurements were conducted at room temperature without magnetic field. The device structure is illustrated schematically in Fig. 2(d). If the CISS signal appears in the $NbSi_2$ slurry, the device will work as follows, as demonstrated in chiral single crystals[11),12)]: A longitudinal electric current applied to the disilicide slurry induces spin polarization due to the CISS effect. The Pt electrode absorbs spin-polarized electrons due to the difference in the spin-dependent chemical potential between the $NbSi_2$ slurry and the Pt electrode. The spin current is converted into a transverse electrical current in the Pt electrode due to the inverse SHE, which eventually induces the transverse voltage V_{xy}.

The inverse CISS (ICISS) signal would be also

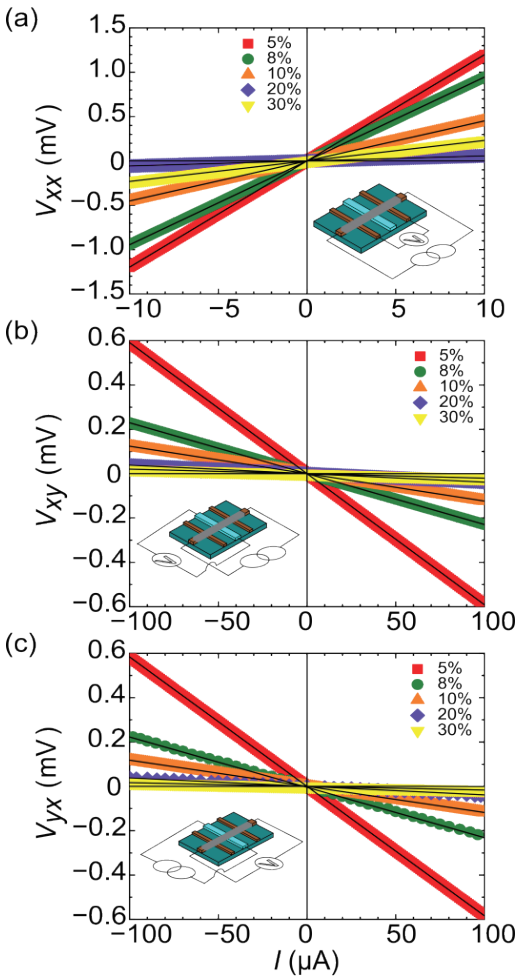

Fig. 3 A dataset of the I-V characteristics for the $NbSi_2$ slurry measured at room temperature without magnetic field. The longitudinal voltage V_{xx} (a), transverse voltage V_{xy} (b) and V_{yx} (c) are taken in the $NbSi_2$ slurry samples with different silver weight percentages. The measurement setups are illustrated in the insets.

detectable in the same device by the following steps: The transverse electric current is applied to the Pt electrode. Due to the SHE, the spin current is produced in an orthogonal direction to the charge current and then diffuses into the $NbSi_2$ slurry. The spin-polarized charge current flows through the slurry via the ICISS and is detected as a longitudinal voltage V_{yx}.

3. Electrical transport measurements

Figure 3(a) illustrates the I-V characteristics of the $NbSi_2$ slurry samples with the silver weight percentages of 5%, 8%, 10%, 20%, and 30% at room temperature in zero magnetic field. The longitudinal voltage V_{xx} shows a linear dependence within a current range of ± 10 μA, giving the Ohmic electrical resistivity for all the samples investigated. As the silver weight percentage in the $NbSi_2$ slurry increases from 5% to 20%, the electrical resistivity gradually decreases from 16 to 0.75

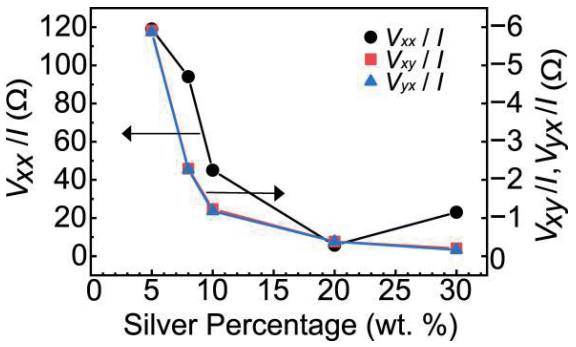

Fig. 4 V_{xx}, V_{xy} and V_{yx} as a function of the silver weight percentage in the $NbSi_2$ slurry.

Ωcm. These resistivity values are much higher than 35 μΩcm reported for bulk single crystals[12]. At 30% silver weight, the obtained electrical resistivity is 3 Ωcm, which is slightly larger than those at lower silver weight percentages. This sudden increase in the longitudinal resistivity at 30% may be attributed to an enhanced influence of the grain boundary between $NbSi_2$ particles in the slurry, which hampers a smooth control of the resistivity value.

The V_{xy} and V_{yx} data are illustrated in Figs. 3(b) and 3(c), respectively. Both measurements were conducted within a current range of ±100 μA with the $NbSi_2$ slurry samples at 5%, 8%, 10%, 20%, and 30%. All the data show negative-slope dependences when the signals appear. V_{xy} and V_{yx} have the same polarity and nearly identical signal amplitudes. These results obtained with the $NbSi_2$ slurry samples are likely to be qualitatively consistent with those for the single crystals[12]. This feature is also consistent that grown single crystals of $NbSi_2$ have a preferred handedness[29] even though they give some chirality domains in the crystals[12]. Moreover, to evaluate whether the observed transverse voltage originates from geometric misalignment of the platinum electrode or from intrinsic effects in various $NbSi_2$ slurry samples, the misalignment angle required for generating the observed electrical signal intensities is compared with the actual misalignment estimated from the optical photographs of the fabricated device. The former values range from 1.39 to 3.83 degrees, while the latter value is less than 0.72 degrees. Thus, the geometric misalignment alone cannot fully account for the observed transverse voltage. This supports the existence of an additional contribution to the transverse voltage generation.

Interestingly, as the silver weight percentage in the $NbSi_2$ slurry samples increases, both the longitudinal and transverse signals decrease monotonically, as shown in Fig. 4. More precisely, V_{xy} and V_{yx} signals keep decreasing while the V_{xx} signal increases in the $NbSi_2$ slurry samples with the silver weight percentages from 20% to 30%. This discrepancy of the behavior between the longitudinal and transverse signals supports the interpretation that the V_{xy} and V_{yx} signals are not simply a result of Pt electrode misalignment,

which would be expected to correlate with the longitudinal voltage V_{xx}, but instead may arise from chirality-driven spin polarization in the $NbSi_2$ particles within the $NbSi_2$ slurry. The present data may indicate that the $NbSi_2$ polycrystalline powders exhibit both direct and inverse CISS effects, as discussed in the previous literature[14),15)].

4. Conclusion

In summary, we studied the electrical transport behavior in chirality-uncontrolled $NbSi_2$ slurry samples prepared by varying silver weight percentages. The local configuration exhibited the longitudinal resistance and transverse voltage at room temperature without magnetic field. The transverse voltage responses exhibit a silver percentage dependence. Interestingly, the observed transverse signals in the local configuration gradually decrease as the percentage of silver weight increases in all the disilicide slurry samples. This decreasing behavior of transverse signals may be attributed to achiral impurity in the disilicide slurry samples. Moreover, despite the uncontrollable handedness in our disilicide slurry samples, the present result may indicate the occurrence of chirality-driven spin polarization response in disilicide powders in the slurry. These findings lay a foundation and provide a methodology for future research, suggesting that the use of chirality-controlled powders could ultimately facilitate the CISS detection. Such work will pave the way for the direct pasting of chiral powders onto solid substrates, which could be replaced by flexible ones and may lead to the promotion of cost-effective chirality-based flexible devices in the future.

Acknowledgements This work was supported by JSPS KAKENHI Grant Nos. 22H01944, 23H01870 and 23H00091. MUK appreciates the support from the Ministry of Education, Culture, Sports, Science and Technology -Japan, through the Japanese Government (Monbukagakusho) Scholarship (MEXT, 2023-2026).

References

1) S. Maekawa, E. Saitoh, S. O. Valenzuela and T. Kimura (Eds.), *Spin Current*, 2nd ed. (Oxford Univ. Press, Oxford, 2017).
2) S. A. Wolf, D. D. Awschalom, R. A. Buhrman, J. M. Daughton, V. S von Molnár, M. L. Roukes, A. Y. Chtchelkanova and D. M. Treger: *Science*, **294**, 1488 (2001).
3) I. Žutić, J. Fabian, and S. D. Sarma: *Rev. of Mod. Phys.*, **76**, 323 (2004).
4) M. I. Dyakonov and V. I. Perel: *Sov. Phys. JETP Lett.*, **13**, 467 (1971). J. E. Hirsch: *Phys. Rev. Lett.*, **83**, 1834 (1999).
5) S. O. Valenzuela and M. Tinkham: *Nature* **442**, 176 (2006). E. Saitoh, M. Ueda, H. Miyajima, and G. Tatara: *Appl. Phys. Lett.* **88**, 182509 (2006). T. Kimura, Y. Otani, T. Sato, S. Takahashi, and S. Maekawa: *Phys. Rev. Lett.*, **98**, 156601 (2007).
6) E. L. Ivchenko and G. E. Pikus: *Sov. Phys. JETP Lett.*, **27**, 604 (1978). V. M. Edelstein: *Solid State Commun.*, **73**, 233 (1990).
7) K. Ray, S. P. Ananthavel, D. H. Waldeck, and R. Naaman: *Science*, **283**, 814 (1999).
8) I. Carmeli, V. Skakalova, R. Naaman, and Z. Vager: *Angewandte Chemie*, **114**, 787 (2002).
9) B. Göhler, V. Hamelbeck, T. Z. Markus, M. Kettner, G.F. Hanne, Z. Vager, R. Naaman and H. Zacharias: *Science*, **331**, 894 (2011).
10) D. Mishra, T. Z. Markus, R. Naaman, M. Kettner, B. Göhler, H. Zacharias, and C. Fontanesi: *Proc. Natl. Acad. Sci. USA.*, **110**, 14872 (2013).
11) A. Inui, R. Aoki, Y. Nishiue, K. Shiota, Y. Kousaka, H. Shishido, D. Hirobe, M. Suda, J. Ohe, J. Kishine, H. Yamamoto and Y. Togawa: *Phys. Rev. Lett.*, **124**, 166602 (2020).
12) K. Shiota, A. Inui, Y. Hosaka, R. Amano, Y. Onuki, M. Hedo, T. Nakama, D. Hirobe, J. Ohe, J. Kishine, H. M. Yamamoto, H. Shishido and Y. Togawa: *Phys. Rev. Lett.*, **127**, 126602 (2021).
13) K. Ohe, H. Shishido, M. Kato, S. Utsumi, H. Matsuura, and Y. Togawa: *Phys. Rev. Lett.* **132**, 056302 (2024).
14) H. Shishido, R. Sakai, Y. Hosaka and Y. Togawa: *Appl. Phys. Lett.*, **119**, 182403 (2021).
15) H. Shishido, Y. Hosaka, K. Monden, A. Inui, T. Sayo,Y. Kousaka and Y. Togawa: *J. Chem. Phys.*, **159**, 064502 (2023).
16) F. Garnier, R. Hajlaoui, A. Yassar and P. Srivastava: *Science*, **265**, 1684 (1994).
17) Y. K. Chang and F. C. Hong: *Nanotechnology*, **20**, 195302 (2009).
18) R. R. Søndergaard, M. Hösel and F. C. Krebs: *J. Polym. Sci. B, Polym. Phys.*, **51**, 16 (2013).
19) S. Khan, L. Lorenzelli and R. S. Dahiya: *IEEE Sens. J.*, **15**, 3164 (2015).
20) K. Takei, W. Honda, S. Harada, T. Arie and S. Akita: *Adv. Healthc. Mater.*, **4**, 487 (2015).
21) G. Dai, Q. Zhan, Y. Liu, H. Yang, X. Zhang, B. Chen and R. W. Li: *Appl. Phys. Lett.*, **100**, 122407 (2012).
22) A. Bedoya-Pinto, M. Donolato, M. Gobbi, L. E. Hueso and P. Vavassori: *Appl. Phys. Lett.*, **104**, 062412 (2014).
23) J. Y. Chen, Y. C. Lau, J. M. D. Coey, M. Li and J. P. Wang: *Sci. Rep.*, **7**, 42001 (2017).
24) Q. Yang, Y. Cheng, Y. Li, Z. Zhou, J. Liang, X. Zhao, Z. Hu, R. Peng, H. Yang and M. Liu: *Adv. Electron. Mater.*, **6**, 2000246 (2020).
25) M. S. Ansari, M. H. D. Othman, M. O. Ansari, S. Ansari and N. Sazali: *Mater. Sci. Eng. B*, **265**, 115033 (2021).
26) J. A. Albro, N. T. Garrett, K. Govindaraj, B. P. Bloom, N. L. Rosi and D. H. Waldeck: *ACS Nano*, **19**, 17941 (2025).
27) C. Wang, Z. R. Liang, X. F. Chen, A. M. Guo, G. Ji, Q. F. Sun and Y. Yan: *Phys. Rev. Lett.*, **133**, 108001 (2024).
28) U. Gottlieb, A. Sulpice, R. Madar and O. Laborde: *J. Phys.: Condens. Matter*, **5**, 8755 (1993).
29) H. Sakamoto, A. Fujii, K. Tanaka and H. Inui: *Acta Mater.*, **53**(1), 41 (2005).

Received Dec. 09, 2025; Revised Dec. 27, 2025; Accepted Jan. 19, 2026

J. Magn. Soc. Jpn., **50**, 43-46 (2026) <Letter>

Structural symmetry and magnetoresistance in epitaxial Fe/Ru/Co multilayers

Y. Suzuki*, T. Hattori*, K. Hayashi*, S. Iihama*, and T. Moriyama*,**
*Department of Materials Physics, Nagoya University, *Nagoya, Aichi 464-8603, Japan*
**Research Center for Crystalline Materials Engineering, Nagoya University, *Nagoya, Aichi 464-8603, Japan*

Magnetic and electrical properties are associated with the structural symmetry of the system. Recent spintronics finds various intriguing physics, such as spin orbit torque, skyrmions, and altermagnetism, rooted in structures with broken or low symmetry. In this work, we investigate epitaxial Fe/Ru/Co multilayers in which the crystalline orientations of the Fe and the Co layers are deliberately made different while they are antiferromagnetically coupled. These synthetic antiferromagnets exhibit resistance variations with the external field which are incomprehensible with conventional magnetoresistances. The results open a possible avenue for creating synthetic magnetism with controlled structural symmetries.

Keywords: spintronics, magnetic multilayers, synthetic antiferromagnet, magnetoresistance, thin film

1. Introduction

Structural symmetry is one of the important factors in modern spintronics. Non-equilibrium spintronic phenomena such as the spin Hall effect (SHE)[1,2] and the spin orbit torque (SOT)[3~6] often manifest more significantly in structures having broken inversions. Ferromagnet (FM)/heavy metal (HM) thin film bilayers, in which the structural inversion is considered broken at the FM/HM interface, are an essential platform for the SHE and SOT where the HM can be Pt, Pd, W, Ta, and so on having a large spin orbit interaction.

On the other hand, structural symmetry also impacts the equilibrium magnetic orders in the magnetic system. Dzyaloshinskii-Moriya interaction (DMI)[7,8] is one of the consequences of the broken structural symmetry which is described by the energy of the spin interaction as $E_{\mathrm{DM}} = -\mathbf{D}\cdot(\mathbf{S}_i \times \mathbf{S}_j)$ where $\mathbf{S}_i$ and $\mathbf{S}_j$ are the neighboring local spins and $\mathbf{D}$ is the Dzyaloshinskii-Moriya (DM) vector. DM interaction was first argued for the canted spins in a hematite (α-Fe_2O_3) where the crystalline symmetry allows the antisymmetric exchange interaction on top of the symmetric exchange interaction, or Heisenberg interaction $E_{\mathrm{Heis}} = -J(\mathbf{S}_i \cdot \mathbf{S}_j)$ where J is the exchange constant. The DMI can be observed not only in the bulk crystal with a specific symmetry but also in the thin film multilayer structures having broken inversion symmetry such as ferromagnet/heavy metal bilayers[9]. This so-called *interfacial* DM interaction acts between the local spins within the ferromagnetic layer via a non-magnetic atom with a strong spin orbit coupling in the heavy metal layer. When the interaction is sufficiently strong, it creates chiral spin textures such as skyrmions and chiral domain walls which are of intense interest in spintronic devices[7,10,11]. DMI in combination with SOT indeed can raise the spintronic device that moves and modifies those chiral spin textures by electric currents.

Recent research extends to magnetic systems with more explicit breaking of the structural symmetry in more scalable manner compared to those relying on the symmetry breaking at a single interface discussed above. Pt/Co/Ta multilayer systems are one of the examples[12]. Since polarity of the SHE angle of Pt is opposite to that of Ta, and the DM vector polarity is opposite between the Pt/Co interface and the Co/Ta interface, both DMI and SHE are therefore scalable with the total thickness of the superlattice. While this way of breaking the structural symmetry could give more control of DMI strength as well as the SHE by trying different material combinations, structural symmetry breaking is always given in the direction parallel to the film normal and it is, in principle, never possible to vary the structural symmetry in the directions in the film plane.

Structural symmetry is also a main focus of the recently emerged altermagnetism. Altermagnetic crystals have a combined feature of both ferromagnets and antiferromagnets. The local spins are antiferromagnetically coupled, but due to the peculiar crystalline symmetry surrounding the local spins the electrons running in the material exhibit a spin polarization unlike the conventional antiferromagnets[13]. Like the synthetic ferromagnets[7,14] and synthetic antiferromagnets[15], how to realize the artificial altermagnets is another interesting question. It is therefore of great importance to seek ways to artificially break structural symmetries in more controllable and scalable manner.

In this work, artificial controlling of structural symmetries is sought in magnetic multilayers, which could potentially lead to an idea of *synthetic* altermagnets. We carefully design the crystalline orientations of Fe/Ru/Co multilayers by epitaxial film growth and characterize the structural symmetry,

Corresponding author: T. Moriyama
(e-mail: moriyama.takahiro.a4@f.mail.nagoya-u.ac.jp).

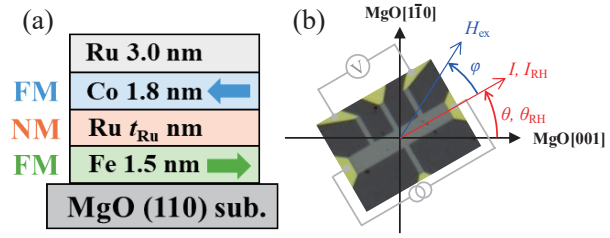

Fig. 1 (a) Schematic illustration of the layer structure. (b) Image of the Hall cross patterned sample for spin transport measurements and definition of the RHEED beam azimuth angle θ_{RH}, the angle of current flow θ with respect to the MgO[001] direction, and the field angle φ with respect to the current direction θ.

magnetic properties, and electrical properties.

2. Methods

Fe 1.5 nm/Ru t_{Ru} = 0.8 ~ 1.7 nm/Co 1.8 nm/Ta 3.0 nm multilayers were deposited on MgO(110) substrate by magnetron sputtering with the base pressure of 10^{-6} Pa. The layer structure of the sample is shown in Fig. 1(a). The thickness of each ferromagnetic layer was designed so that they have the same total magnetic moment assuming the saturation magnetization of Fe and Co to be 1751 and 1440 emu/cm^3, respectively. The substrate temperature was kept at 500℃ during the deposition of the Fe layer to promote epitaxial growth. All the other layers were deposited at room temperature. t_{Ru} was varied to realize an antiferromagnetic coupling between the ferromagnetic layers. Crystallinity of each layer surface was characterized by the reflection high-energy electron diffraction (RHEED). Magnetization measurements were performed by magneto-optical Kerr effect (MOKE) and superconducting quantum interference device (SQUID). Electrical measurements were performed with the samples patterned into a Hall cross structure as shown in Fig. 1(b). The measurements were performed with various directions and strengths of the magnetic field as well as the direction of current flow with respect to the crystalline axis. The definition of the RHEED beam azimuth angle θ_{RH}, the angle of current flow θ with respect to the MgO[001] direction, and the field angle φ is also in Fig. 1(b). A single layer of Fe and Co deposited on the MgO substrate were also characterized as a control sample. In addition, macro-spin simulations based on the Landau-Lifshitz-Gilbert (LLG) equation were employed to analyze the experimental results.

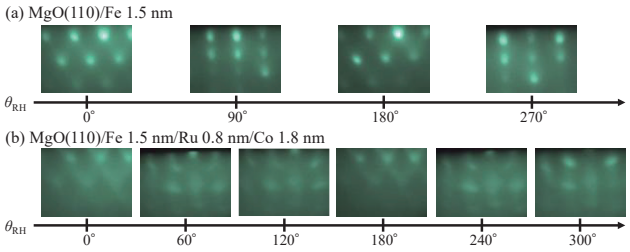

Fig. 2 RHEED patterns for the Fe and Co surfaces.

3. Results & Discussion

Fig. 2 shows RHEED patterns after growing the Fe and Co layers. Fig. 2(a) indicates that the Fe layer is epitaxially grown on the MgO(110) substrate. The patterns show a twofold symmetry with respect to the azimuth angle θ_{RH}. Instead of our initial expectation that Fe(110) would grow on MgO(110), the detailed pattern analysis suggests that the Fe(211) surface is exposed to the surface. This is indeed consistent with previous studies reporting the Fe(211) twin growth on MgO(110) in the similar condition with ours[16]. In any case, it is confirmed that the Fe layer has a twofold crystalline symmetry in the film plane. Although the RHEED spot pattern indicates the presence of atomic-scale roughness, a relatively large interlayer antiferromagnetic coupling is obtained, as discussed in the experimental results presented later. The coupling may be enhanced by reducing the roughness[17]. However, the observed roughness is considered to have no significant effect on the discussion of this study. The Ru layer was then deposited on the Fe surface and subsequently the Co layer. RHEED on the Co surface (Fig. 2(b)) still show an ordered pattern but vaguer than those on the Fe layer, suggesting the single crystallinity is degraded. The patterns lost a twofold symmetry that the Fe layer showed but more sixfold with respect to θ_{RH}, indicating the Co is facing (111). Variation of t_{Ru} = 0.8 ~ 1.7 nm do not change much the RHEED patterns. These observations clearly suggest that upper and bottom

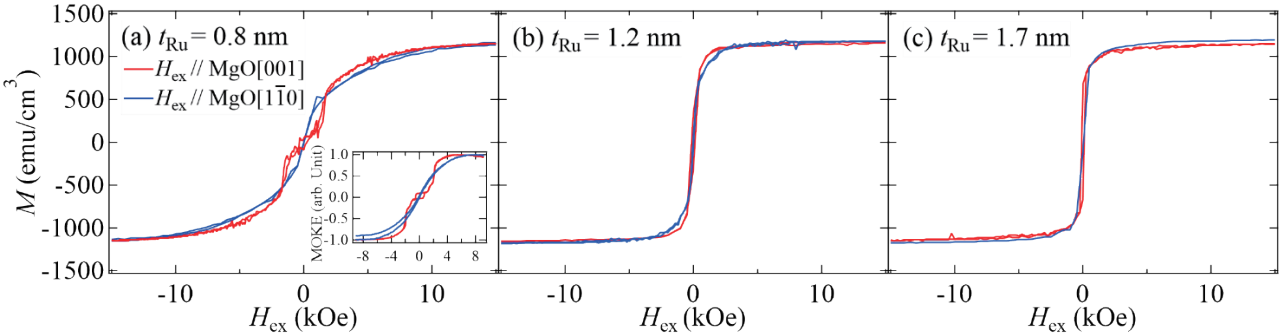

Fig. 3 (a) (b) (c) Magnetization results by SQUID: Results for samples with t_{Ru}= 0.8, 1.2, and 1.7 nm. The inset of Fig. 3(a) presents the magnetization result by MOKE.

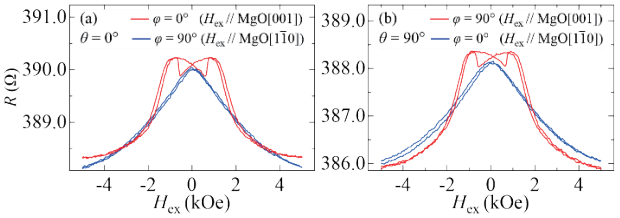

Fig. 4 (a) (b) Magnetoresistance under magnetic field sweep: Measurements were carried out with θ set to 0° and 90°, as defined in Fig. 1(b).

ferromagnetic layers have a global crystal symmetry that is different from each other.

Fig. 3 shows the magnetization measurements performed by using SQUID for t_{Ru} = 0.8, 1.2, and 1.7 nm. The magnetic field was swept along MgO[1 $\bar{1}$ 0] and MgO[001]. First, among different t_{Ru}, the sample with t_{Ru} = 0.8 nm shows the plateau in the low field in the field along MgO[001], indicating achievement of the antiferromagnetic coupling between the Fe and Co layers. The t_{Ru} dependence of the antiferromagnetic coupling strength agrees well with the previous study[18]. The MOKE measurements (the inset of Fig. 3 (a)) more clearly show a stable antiferromagnetic coupling in the field range ± 500 Oe. Note that, due to the MOKE sensitivity for the Fe and Co layers, it shows the hysteresis loop in the low field. The magnetization curves along MgO[1$\bar{1}$0], on the other hand, do not show any plateau, suggesting a relatively strong in-plane magnetic anisotropy probably originating from the twofold symmetry in the Fe layer. These results, together with the RHEED patterns, suggests that the Fe 1.5 nm/Ru 0.8 nm/Co 1.8 nm we grew has a different crystalline symmetry in upper (Co) and bottom (Fe) ferromagnetic layers and they are antiferromagnetically coupled at the same time, which is analogous to the altermagnets.

Fig. 4 shows the resistance as a function of the magnetic field at φ = 0° and 90° with the direction of the current flow θ = 0° and 90°. The resistance change is monotonous with the field along MgO[1 $\bar{1}$ 0] reflecting the corresponding magnetization curves with the giant magnetoresistance (GMR) contribution[19] while it shows some details with the field along MgO[001] around which the plateau is observed in the magnetization curves. The hysteresis observed in the range ± 500 Oe seems to be corresponding to the hysteresis observed in the MOKE measurement, indicating the simultaneous switching of the Fe and Co magnetization (while maintaining the antiferromagnetic coupling) gives rise to additional resistance change. When H_{ex} is applied along MgO[001], a small bowtie shaped hysteresis is observed at low fields ($|H_{ex}| < 1$ kOe) where the MOKE data (inset of Fig. 3(a)) also shows a small hysteresis. We assume that this could be associated with a switching of the Fe (Co) moment while they maintain the antiferromagnetic coupling.

Fig. 5 shows the resistance as a function of the field angle φ at H_{ex} = 2.5 kOe with θ = 0° and 60° for the Fe 1.5 nm/Ru 0.8 nm/Co 1.8 nm as well as the control samples: MgO(110)/Fe 1.5 nm /Ru 3.0 nm and MgO(110)/Ru 0.8 nm/Co 1.8 nm/Ta 3.0 nm. We note that H_{ex} = 2.5 kOe applied in these measurements is out of the range.

The control samples show the resistance change following a $\sin^2\varphi$ function and the φ dependence is invariant regardless of the current direction θ with respect to MgO[001], which is well expected by the anisotropic magnetoresistance (AMR). It should be noted that the Co layer shows the negative AMR[20~22] where the resistance is minimum when the magnetic field is parallel to the current (φ = 0°). On the other hand, the resistance change in Fe 1.5 nm/Ru 0.8 nm/Co 1.8 nm sample shows completely different φ dependence with different θ (compare red and blue line in Fig. 5(a)), which cannot solely be explained by the combination of the Fe and Co AMRs. Since there is a sizable GMR, it is possible that relative angle between the Fe and Co magnetizations varies with φ and it varies the resistance with φ.

To scrutinize the possibility, we conduct an LLG-equation based macro-spin simulation by incorporating the magnetic parameters, such as magnetic anisotropy field of Fe layer : 200 Oe, antiferromagnetic coupling field : 5000 Oe, the saturation magnetization, the AMR ratios for the Fe and Co layers (0.05 % and 0.01 %), the GMR ratio (0.54 %) and the resistivity of each layer estimated from the magnetization curves and the resistance curves. Fig. 6 shows the experimental results with various θ compared to the simulated results. The resistance change for the simulated results is normalized by the maximum resistance variations given by the AMR and GMR ratios. Overall trend of the φ dependence with respect to θ reproduced by the simulations is found to be

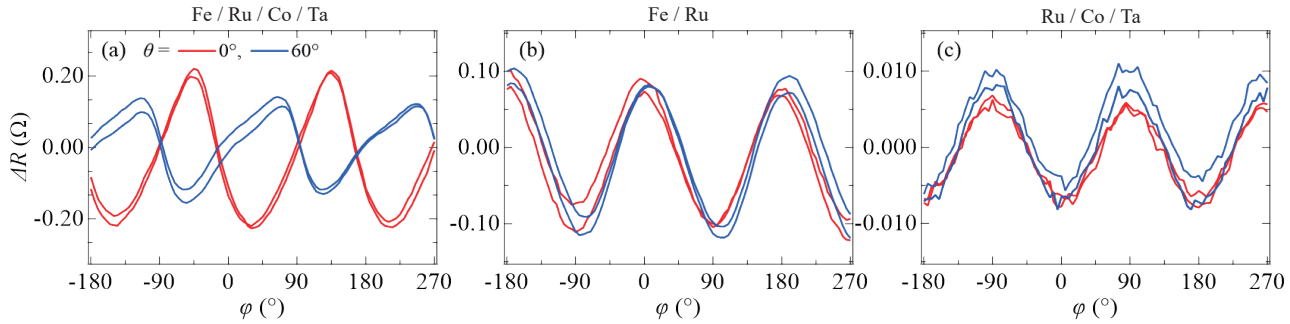

Fig. 5 Magnetoresistance of the multilayer sample and reference samples: The upper figure presents the results for the sample with θ = 0° shown in Fig. 1(b), whereas the lower figure corresponds to the sample with θ = 60°.

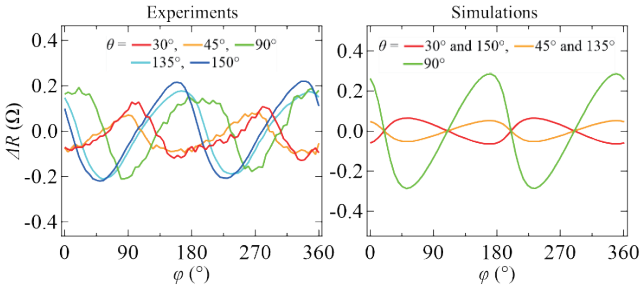

Fig. 6 Comparison between experimental and simulated magnetoresistance results: The resistance of the simulations is normalized. Note that simulated curves for θ=150° and 135° are invisible in the plot because they are completely overlapped with ones for θ=30° and 45°, respectively.

very different from the experimental data. Besides the magnitude of the resistance oscillation, the oscillation phase is very inconsistent with each θ. It should be noted that there could be errors in the simulation parameters estimated by the experimental data which gives errors in the simulation results. Moreover, we do not take into account possible interfacial/interlayer DM interactions in the simulations. Those might influence the magnitude of the resistance oscillation and the subtle shape of the curves, but hardly do the oscillation phase. Since the AMR ratio is very small compared to the GMR's, the simulation results and the experimental results are essentially dominated by the GMR variation due to the relative angle change of the Fe and Co magnetizations with the twofold magnetic anisotropy in the Fe. This comparison reveals that the experimentally obtained resistance change could contain other contributions than those conventional magnetoresistances. Whether or not this is associated with the different crystalline symmetries deliberately created in this sample should need more extensive investigations. Moreover, it could be more interesting to see if there are non-trivial spin transport properties due to the structural symmetries.

4. Summary

We sought to artificially control structural symmetries in magnetic multilayers, which could potentially lead to an idea of synthetic altermagnets. We fabricated epitaxial Fe/Ru/Co multilayers on MgO(110) substrate. It was found that, in a certain deposition condition, the multilayers are epitaxially grown in such a way that the bottom Fe layer has twofold-symmetric Fe(211) orientation and the top Co layer has sixfold-symmetric Co(111). The appropriate Ru thickness simultaneously realizes the antiferromagnetic coupling between the Fe and the Co. These synthetic antiferromagnets show resistance variations with the external field which are incomprehensible with conventional magnetoresistances. While the physical origins of the spin transport properties including the magnetoresistance are still obscure, our demonstrations of the multilayer fabrication open a possible avenue for fabricating synthetic magnetism with controlled structural symmetries.

Acknowledgements This work was supported in part by JST FOREST Program Grant Number JPMJFR2242, JST CREST Grant Number JPMJCR24R5, and JSPS KAKENHI Grants Nos. 23KK0093, 24H02235 and 24K23945.

References

1) M. I. Dyakonov, and V. I. Perel: *Phys. Lett.* A **35**, 459 (1971).
2) J. Sinova, S. O. Valenzuela, J. Wunderlich, C. H. Back, and T. Jungwirth: *Rev. Mod. Phys.* **87**, 1213 (2015).
3) J. E. Hirsch: *Phys. Rev. Lett.* **83**, 1834 (1999).
4) S. Zhang: *Phys. Rev. Lett.* **85**, 393 (2000).
5) I. M. Miron, K. Garello, G. Gaudin, P-J. Zermatten, M. V. Costache, S. Auffret, S. Bandiera, B. Rodmacq, A. Schuhl, and P. Gambardella: *Nature* **476**, 189 (2011).
6) A. Manchon, J. Železný, I. M. Miron, T. Jungwirth, J. Sinova, A. Thiaville, K. Garello, and P. Gambardella: *Rev. Mod. Phys.* **91**, 035004 (2019).
7) I. Dzyaloshinsky: *J. Phys. Chem. Solids* **4**, 241 (1958).
8) T. Moriya: *Phys. Rev.* **120**, 91 (1960).
9) A. Fert, V. Cros, and J. Sampaio: *Nat. Nanotech.* **8**, 152 (2013).
10) A. N. Bogdanov and D. A. Yablonskii: *Sov. Phys. JETP* **68**, 101 (1989).
11) A. Fert, N. Reyren, and V. Cros: *Nat. Rev. Mater.* **2**, 17031 (2017).
12) S. Woo, M. Mann, A. J. Tan, L. Caretta, and G. S. D. Beach: *Appl. Phys. Lett.* **105**, 212404 (2014).
13) L. Šmejkal, J. Sinova, and T. Jungwirth: *Phys. Rev. X* **12**, 040501 (2022).
14) W. J. Waring, Y. Li, C. Moutafis, I. J. Vera-Marun, and T. Thomson: *Phys. Rev. B* **104**, 014419 (2021).
15) R. A. Duine, Kyung-Jin Lee, Stuart S. P. Parkin, and M. D. Stiles: *Nat. Phys.* **14**, 217 (2018).
16) K. Shikada, K. Tabuchi, M. Ohtake, F. Kirino, and M. Futamoto: *J. Mag. Soc. Jpn.* **32**, 296 (2008).
17) J. Kudrnovský, V. Drchal, I. Turek, M. Šob, and P. Weinberger: *Phys. Rev. B* **53**, 5125 (1996).
18) S. S. P. Parkin, N. More, and K. P. Roche: *Phys. Rev. Lett.* **64**, 2304 (1990).
19) A. Fert: *Rev. Mod. Phys.* **80**, 1517 (2008).
20) Y. Sakuraba, S. Kokado, Y. Hirayama, T. Furubayashi, H. Sukegawa, S. Li, Y. K. Takahashi, and K. Hono: *Appl. Phys. Lett.* **104**, 172407 (2014).
21) A. Kobs, and H. P. Oepen: *Phys. Rev. B* **93**, 014426 (2016).
22) R. Toyama, S. Kokado, K. Masuda, Z. Li, V. K. Kushwaha, T. T. Sasaki, L. S. R. Kumara, T. Koganezawa, H. Tajiri, T. Yamazaki, M. Kotsugi, Y. Iwasaki, and Y. Sakuraba: *Phys. Rev. Mater.* **7**, 084401 (2023).

Received Dec. 8, 2025; Accepted Jun. 5, 2026

J. Magn. Soc. Jpn., **50**, 47-51 (2026) <Paper>

Performance Comparison of Interior Permanent Magnet Synchronous Motors with Amorphous Alloy and Silicon Steel Stator Core

İbrahim Çirozlar, Kenji Nakamura
Graduate School of Engineering, Tohoku University, *6-6-11 Aoba Aramaki Aoba-ku, Sendai 980-8579, Japan*

The global push towards electrification, particularly in the automotive and aerospace sectors, necessitates the development of electric motors with higher efficiency and power density. A primary limiting factor in high-speed permanent magnet synchronous motors (PMSMs) is the core loss in the stator. This study presents an experimental performance comparison of an interior permanent magnet synchronous motor (IPMSM) using stator cores made from an advanced amorphous alloy and a conventional silicon steel core. To conduct this evaluation, two motors of identical design were constructed: one with an amorphous alloy core (AMO), and one with a non-oriented silicon steel core (NGO). The motors were tested under various load conditions at 12,600 rpm using maximum torque per ampere (MTPA) control. The results demonstrate that the IPMSM with the AMO stator core achieved a significant reduction in iron loss of up to 72% compared to the one with the NGO stator core, while maintaining nearly identical torque density. This substantial loss reduction led to an overall efficiency improvement of approximately 3.1%. These findings confirm that amorphous alloys are a highly effective core material for improving the efficiency of high-speed IPMSMs by drastically reducing the iron loss.

Key words: Interior permanent magnet synchronous motor (IPMSM), amorphous alloy, high-speed

1. Introduction

The global transition towards electrification is rapidly accelerating, driven by a collective push for greater energy efficiency and reduced carbon emissions in key sectors such as electric vehicles (EVs), aerospace, and advanced industrial automation. This paradigm shift has created an unprecedented demand for electric motors that are not only more powerful but also significantly more efficient. To achieve higher power density, it is often necessary to push operating speeds and frequencies to new limits, where iron losses increase nonlinearly and can become the crucial source of inefficiency and heat generation. This challenge necessitates the exploration of advanced core materials capable of mitigating the iron losses.

To overcome these limitations, advancements in this field often follow two primary paths in materials science: the enhancement of permanent magnets and the improvement of soft magnetic materials. Previous work by our research group has focused on the former, demonstrating that the strategic use of polar-anisotropic bonded magnets within an inset rotor topology can significantly improve the efficiency of high-speed motors [2], and that the world's first Sm-Fe-N/Fe-N hybrid bonded magnet motor exhibits sufficient performance [3]. Building upon that foundation, the present study shifts its focus to the latter approach—the application of advanced soft magnetic materials.

Recent studies have increasingly highlighted amorphous alloys as a promising alternative to conventional silicon steels. For instance, Zeng et al. analyzed the performance of PMSMs with amorphous alloy and silicon steel stators, demonstrating that the low-loss characteristics of amorphous alloys become particularly advantageous at higher operating speeds [4]. In the context of thermal reliability, Li et al. investigated a yokeless and segmented armature axial-flux in-wheel motor with an amorphous alloy stator, showing through both simulation and prototype validation that the temperature rise remained within safe operational limits for EV applications [5].

Experimental studies have also revealed important enhancements in applying amorphous alloy cores. Ismagilov et al. demonstrated that while amorphous alloy stators offer low loss advantages, in unmanned aerial vehicle (UAV) motors their performance converges with that of conventional silicon steel beyond approximately 6500 rpm due to saturation effects [6]. Similarly, Ou et al. found that in a DC-excited flux-modulated motor, amorphous alloys drastically reduced high-frequency core losses as the copper losses increased slightly, confirming their potential for high-speed applications [7]. Kolano et al. further validated this experimentally by constructing a high-speed PMBLDC motor with an amorphous stator core featuring half-open slots, achieving nearly 90% efficiency across a wide torque range [8].

However, practical challenges remain. Manufacturing stresses can significantly degrade the expected benefits of amorphous alloys, as shown by Okamoto et al., who reported that while an IPMSM with an amorphous alloy stator achieved a 38% reduction in core loss, this was considerably lower than the approximately 65% predicted by simulations [9]. Nevertheless, long-term validation has further reinforced the advantages of amorphous alloys. Enomoto et al. demonstrated that amorphous alloy stator components yielded the highest efficiency and lowest core loss compared to motors using either conventional silicon steels or soft magnetic composites [10].

Taken together, these studies highlight both the potential and the limitations of amorphous alloys in high-speed, high-efficiency motors. Building on this foundation, the primary objective of the present work is to investigate and quantify the performance of high-speed IPMSM prototypes with an amorphous alloy stator core and a conventional silicon steel stator core. The evaluation begins with measurements of electromagnetic characteristics of the prototypes such as winding resistance, inductance and back-EMF. Subsequent experiments examine torque – current phase angle characteristics and torque characteristics under maximum torque per ampere (MTPA) control. Finally, after conducting a mechanical loss test using an identical demagnetized rotor,

Corresponding author: İbrahim Çirozlar (e-mail: cirozlar.ibrahim.r2@dc.tohoku.ac.jp).

detailed loss distributions and efficiency maps of the prototypes are compared.

2. Research Procedures

2.1 Motor Specifications

To evaluate the impact of amorphous alloys on motor performance, a comparative experimental study was conducted using two IPMSM prototypes. As specified in Fig. 1, to ensure a direct and fair comparison, two prototypes were constructed with identical stator and rotor geometries. The baseline motor was fabricated with a conventional non-oriented silicon steel (NGO) stator core. The second motor utilized amorphous alloy stator core (AMO).

Fig. 2 provides an external view of the prototype motor. Additionally, a third prototype, mechanical test motor (MTM), was prepared to precisely quantify mechanical loss. The MTM shared the same structural design but was assembled without windings and with demagnetized magnets. All prototypes employed an identical motor structure, which included a silicon steel core and Nd permanent magnets.

2.2 Experimental Setup

Fig. 3 presents the general test bench configuration. The setup consisted of a hysteresis brake (500 mN·m, 30,000 rpm), a DC voltage source (0–80 V, 0–80 A, 800 W), a power meter for measuring the input power of the motor, an inverter, and an LCR meter for measuring winding resistance and inductance. A motor analyzer was employed to record output parameters such as torque and speed through the hysteresis brake, while a thermocouple was used to monitor the winding temperature. The inverter was controlled via a PC interface, through which speed commands and current phase angles were applied. Motor operation was synchronized using an encoder to provide accurate rotor position feedback for drive control.

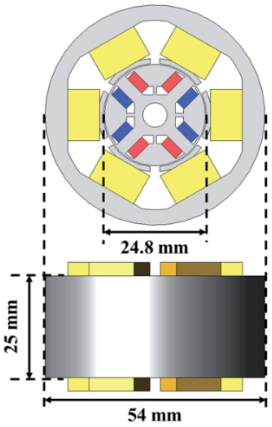

	Winding	Concentrated
Structure	Poles/Slots	4/6
	Airgap (mm)	0.3
Stator	Core Material	AMO: Amorphous alloy sheet (Sing. Core) NGO: Silicon steel
Rotor	Core Material	Silicon steel
Magnet	Number	8
	Material	Nd Magnet

Fig. 1 Specifications of the IPMSM prototypes.

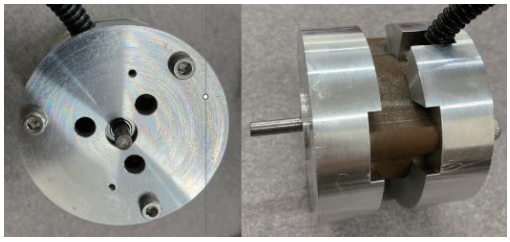

Fig. 2 External view of the prototypes.

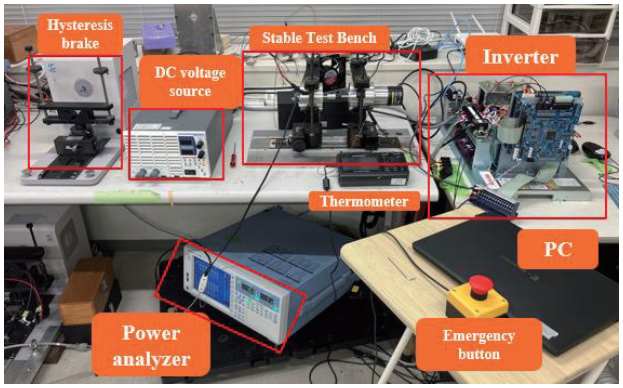

Fig. 3 Appearance of test bench.

2.3 Preparation Prior to Experiment

Table 1 shows the experimental procedure for evaluating the prototype motors. The process was divided into six steps; first three are to acquire electromagnetic characteristics of the prototypes and their mechanical loss value.

Initially, the fundamental motor constants were verified. The three-phase winding resistance (R_a) and the d- and q-axis inductances (L_d, L_q) were precisely measured for each prototype using an LCR meter. This step ensured the consistency of the winding and assembly across the prototypes and provided accurate parameters.

The magnetic performance was evaluated by measuring the back-EMF. Each motor was driven at a constant speed of 12,600 rpm by an external motor with its terminals open-circuited. The resulting voltage, measured using a power analyzer, was used to determine the flux linkage (Ψ_a), confirming the appropriateness of the magnetic design. Example back-EMF waveforms of the AMO motor are shown in Fig. 4 to clearly illustrate the airgap field distribution for the prototype design.

Table 2 shows the fundamental electromagnetic parameters of the two prototype motors. Their resistances were closely matched, and the measured temperatures correspond to the winding temperature of each motor during the resistance tests. The inductance for the AMO motor was slightly lower than that of the NGO motor, with saliency ratio (L_q/L_d) of 1.7 for the AMO motor compared to 1.8 for the NGO motor.

Table 1 Test procedures.

	Steps	Objective	Instruments
①	Winding resistance & inductance	3-phase balance check Motor constant Ra confirmation. Motor constant Ld, Lq confirmation	LCR meter
②	Induced Back-EMF	Understanding the identity and appropriateness of the design Checking Ψa	Power analyzer
③	Mech. loss	Loss separation	Power analyzer
④	Torque – I_d, I_q characteristic	Optimum current phase angle for each current density (MTPA)	Hysteresis break & Power analyzer
⑤	Torque – Current characteristics	Characteristic verification during MTPA control.	Hysteresis break & Power analyzer
⑥	Load loss (MTPA)	Comparison of losses for each core	Hysteresis break & Power analyzer

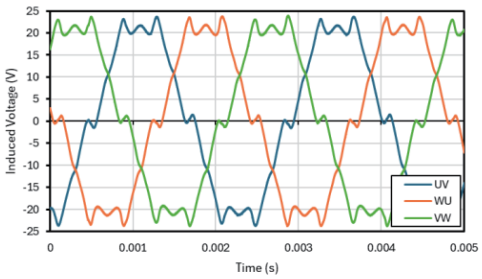

Fig. 4 Observed back-EMF waveforms of the AMO motor.

Table 2 Electromagnetic parameters of the AMO and NGO motor.

Frequency (Hz) [speed (rpm)]	Motor	Resistance (mΩ) (DC)	Inductance L_d (mH)	Inductance L_q (mH)	Saliency ratio L_q/L_d	ψ_a (mWb)	Temperature (°C)
420 [12,600]	AMO	30.4	0.196 ±0.001	0.336 ±0.001	1.7	10.7	22.5
	NGO	30.8	0.215 ±0.003	0.38 ±0.003	1.8	10.9	26.0

Fig. 5 illustrates the configuration of the mechanical loss test, which consists of a drive motor and an MTM. First, the drive motor was operated under no-load conditions, and its input power was recorded. Next, the MTM was coupled to the drive motor shaft, and the input power of the drive motor was measured again. Each test was conducted three times, with a duration of 30 minutes per trial, to ensure repeatability. A view of the experimental setup is provided in Fig. 6.

The average mechanical loss was determined from the difference in input power between the two test conditions. For the coupled system, the drive motor's input power represented the combined losses of both machines; isolating the MTM contribution yielded an average mechanical loss of approximately 4.4 W at the rated speed of 12,600 rpm, as shown in Table 3. During the tests, an identical encoder was mounted

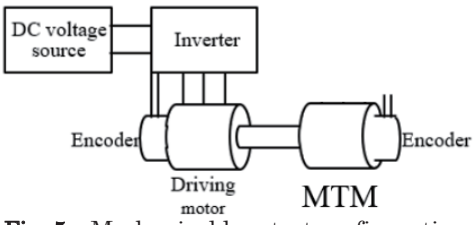

Fig. 5 Mechanical loss test configuration.

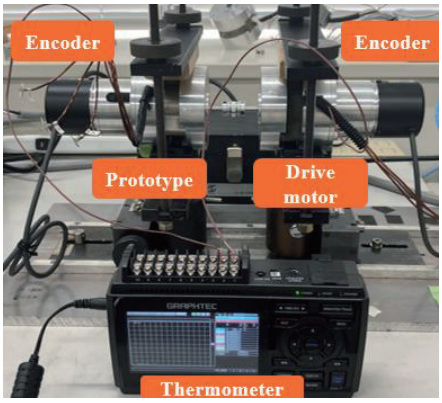

Fig. 6 Mechanical loss test setup view.

Table 3 Measured average mechanical loss at 12,600 rpm.

Input Powers P_{in}(W)		Mech. Loss (W)
MTM	Driv. Mtr.	(MTM) – (Driv. Mtr.)
9.6	5.2	4.4

at the end of the MTM to ensure accuracy, as shown in Fig. 6. Result of this mechanical loss test was treated as constant and was subtracted from the total measured losses in all subsequent load tests for each of the prototypes.

3. Test Results

3.1 Torque–current phase angle characteristics of the NGO and AMO motors

A key aspect of the performance evaluation under MTPA is the determination of the optimal current phase angle (β_{Tmax}) required to achieve the highest torque for a given current.

To evaluate performance under load, the torque characteristics were mapped. Each motor was coupled to a hysteresis brake and operated at various current densities (2, 4, 6, and 8 A/mm^2). At each load point, the current phase angle was systematically adjusted to identify the optimal angle for MTPA operation. The torque-current and torque-efficiency relationships under MTPA control were then recorded using the power analyzer and torque meter.

Fig. 7 illustrates the experimental results of the NGO and AMO motor at current densities of 2, 4, 6 and 8 A/mm^2, while Table 4 summarizes the optimal current phase angles for both prototypes across the full range of tested current densities.

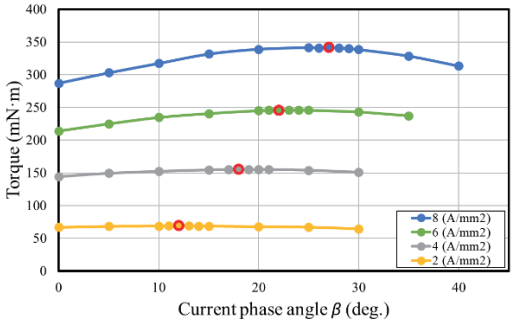

(a) NGO

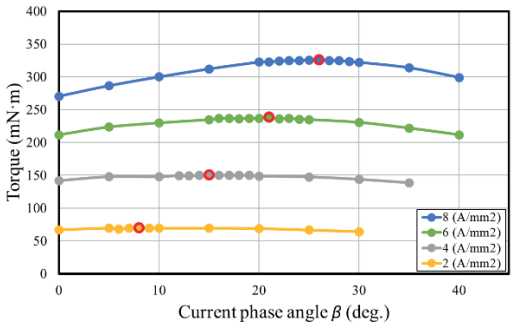

(b) AMO

Fig. 7 Torque–current phase angle characteristics of the NGO and AMO motors (MTPA points are marked in red).

Table 4 Current phase angle points for the MTPA drive for each prototype.

Current Density (A/mm²)	Current phase angle β_{Tmax} (deg.)	
	AMO	NGO
2	8	12
4	15	18
6	21	24
8	26	28

3.2 Experimental Results under MTPA control

The characteristics of the prototypes were evaluated across a range of load points under MTPA control. A critical aspect of this evaluation was to confirm that the torque density was preserved with the new core material.

Fig. 8(a) shows torque characteristics under MTPA control. The figure reveals that the measured torques of two prototypes were nearly identical. This result demonstrates that substituting silicon steel with amorphous alloy did not compromise the motor's torque production capability.

Fig. 8(b) indicates the copper losses. It was found to be nearly identical across two motors, which is expected given their similar winding resistances and operating currents.

Fig. 8(c) compares the iron losses of both motors. The iron loss is separated from the total loss as follows: First, the mechanical loss (W_m) due to friction and windage was quantified by testing the dedicated MTM, as described in section 2.3. Subsequently, during the load tests of the main prototypes, the electrical input (P_{in}) and mechanical output (P_{out}) powers were measured. As in Eq. (1), the total measured losses (W_{total}) were then calculated as the difference between P_{in} and P_{out} :

$$W_{\mathrm{total}} = P_{\mathrm{in}} - P_{\mathrm{out}} \tag{1}$$

The total losses were then separated into their primary components: copper loss (W_c), iron loss (W_i), and mechanical loss (W_m). As in Eq. (2), the copper loss was calculated using the measured winding resistance and phase current:

$$W_{\mathrm{c}} = 3I_{\mathrm{rms}}^2 R_{\mathrm{a}} \tag{2}$$

The measured mechanical loss (W_m) is subtracted, allowing for the experimental determination of the iron loss using Eq. (3):

$$W_{\mathrm{i}} = W_{\mathrm{total}} - W_{\mathrm{c}} - W_{\mathrm{m}} \tag{3}$$

It is evident that at every measured load point, the AMO motor exhibited dramatically lower iron loss than the NGO motor. For instance, at a load torque over 300 mN·m, corresponding to 8 A/mm², the iron loss of the NGO motor was 23.6 W, whereas that of the AMO motor was only 7.9 W. This represents a remarkable iron loss reduction of approximately 66% at higher loads. At lower loads (2 A/mm²), the reduction was even more pronounced, reaching up to 72%.

Finally, Fig. 8(d) represents efficiency. It can be seen that the AMO motor demonstrated a clear advantage over the NGO motor. At the rated torque of approximately 250 mN·m, the NGO motor achieved an efficiency of 91.0%, whereas the AMO motor achieved an efficiency of approximately 94.1%. This represents a significant efficiency improvement of about 3.1% through the change in the stator core material

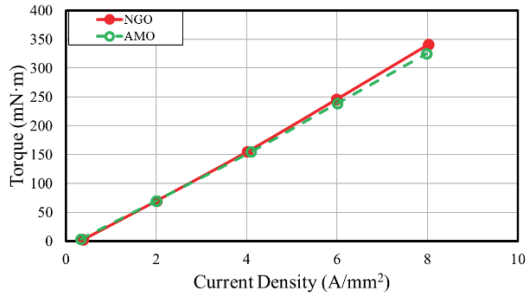

(a)Current density – Torque

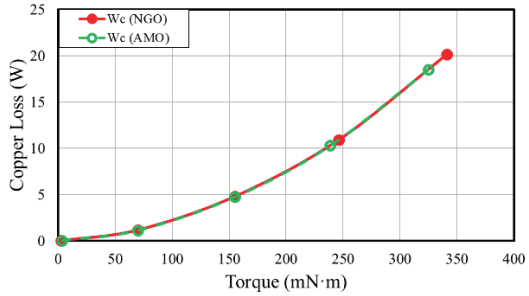

(b) Torque – Copper loss

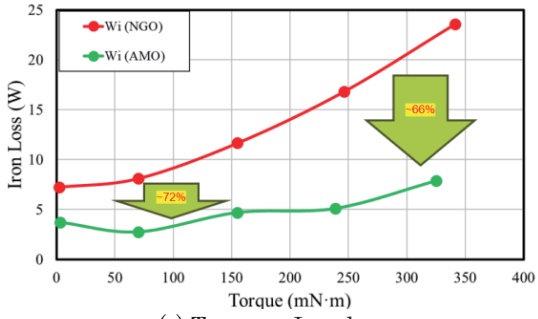

(c) Torque – Iron loss

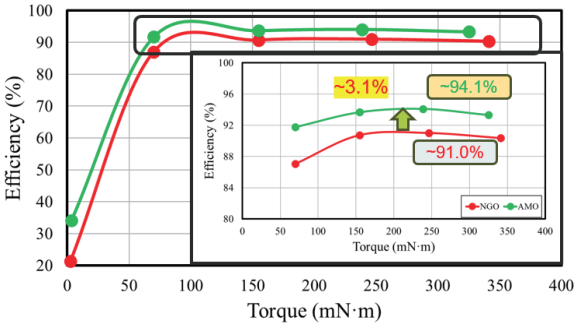

(d) Torque – Efficiency

Fig. 8 Performance comparison of the two prototypes for the MTPA drive.

4. Discussion

The experimental results from this study provide clear and quantitative validation of the benefits of using amorphous alloy stator cores in high-speed IPMSMs. The primary finding of a 3.1% efficiency improvement is directly attributable to the substantial reduction in iron loss, which was lowered by as much as 72% compared to the conventional silicon steel counterpart. This dramatic

decrease in iron loss is consistent with the fundamental properties of amorphous magnetic materials, which possess higher electrical resistivity and lower coercivity, thereby suppressing both eddy current and hysteresis losses, especially at the high electrical frequency of 420 Hz, corresponding to the motor's rated speed of 12,600 rpm.

The loss separation analysis underscores the significance of this finding. With mechanical and copper losses being identical across all prototypes, the iron loss emerged as the sole performance differentiator. In the conventional NGO motor, iron loss constituted a significant portion of the total losses, particularly at higher loads. By replacing the silicon steel with an amorphous alloy, this dominant loss component was effectively minimized, leading to the observed increase in overall efficiency. This result strongly aligns with the conclusions of simulation-based studies and provides experimental data that surpasses the approximately 38% core loss reduction reported in previous experimental work on a similar amorphous IPMSM [9].

5. Conclusion

In summary, this research provides definitive experimental evidence that the substitution of conventional silicon steel with an amorphous alloy is a highly effective strategy for mitigating core losses and boosting the efficiency of high-speed permanent magnet motors.

The motor with amorphous alloy stator core achieved a peak efficiency of 94.1%, a significant improvement of 3.1% over the 91.0% efficiency of the identical motor with a silicon steel core.

The primary driver for the efficiency gain was a drastic reduction in iron loss. The AMO motor has 66% to 72% lower iron loss result compared to the NGO motor across the entire load range at the speed of 12,600 rpm.

Acknowledgements This work was supported by WISE Program for AI Electronics at Tohoku University and MEXT Program: Data Creation and Utilization-Type Material Research and Development Project Grant Number JPMXP1122715503.

References

1) IEA: *Global EV Outlook 2025* (IEA, Paris, 2025).
2) Y. Uchiyama, K. Nakamura, O. Ichinokura, H. Goto, and H. J. Guo: *T. Magn. Soc. Jpn. (Special Issues),* **4**, 67 (2020).
3) İ. Çirozlar, S. Murakami, K. Nakamura, T. Ogawa, S. Yamamoto, N. Kobayashi, and H. Yamamoto: *J. Magn. Soc. Jpn*, **49**, 32 (2025).
4) L. Zeng, N. Zhang, Z. Xie, X. Lu, X. Liu, R. Pei: *Proc. 2025 19th Conf. Electr. Mach., Drives Power Syst. (ELMA)*, 1 (2025).
5) T. Li, Y. Liang, Y. Yang, J. Tian, L. Fan; *IEEE Access*, **13**, 48672 (2025).
6) F. R. Ismagilov, R. R. Urazbakhtin, and A. R. Khakimyanov: *Proc. 2024 Int. Ural Conf. Elect. Power Eng. (UralCon)*, 419 (2024).
7) J. Ou, Y. Liu, M. Schiefer, P. Breining, M. Doppelbauer, F. Chai: *Proc. 2018 IEEE Energy Convers. Congr. Expo. (ECCE)*, 1 (2018).
8) R. Kolano, A. Burian, K. Krykowski, J. Hetmanczyk, M. Hreczka, M. Polak, J. Szynowski: *IEEE Trans. Magn.*, **52**, 2003005 (2016).
9) S. Okamoto, N. Denis, and K. Fujisaki: *Proc. 2015 IEEE Int. Electr. Mach. Drives Conf. (IEMDC)*, 208 (2015).
10) Y. Enomoto, M. Ito, H. Koharagi, R. Masaki, S. Ohiwa, C. Ishihara, M. Mita: *IEEE Trans. Magn.*, **41**, 4304 (2005).

Received Oct. 24, 2025; Accepted Jan. 15, 2026

J. Magn. Soc. Jpn., **50**, 52-61 (2026) <Paper>

Study on electromagnetic force and axial uniformity of electromagnetic forming of 2024- aluminum alloy tube based on double magnetic field converter

CHENG Zerui[1],CHENG Jianghong[1],AHMED ABU-SIADA[2],LI Mengyao[1,3],ZHANG Jinrong[1,4],CAO Cheng[1]

1. College of Electrical Engineering and New Energy China Three Gorges University, *Yichang, 443002, China*
2. Department of Electrical and Computer Engineering, Curtin University, *Perth, WA 6102, Australia*
3. State Grid Henan Electric Power Co., Ltd. Luoyang Power Supply Company, *Luoyang, 438000, China*
4. State Grid Gansu Electric Power Co., Ltd. Ultra High Voltage Branch, *Lanzhou, 730000, China*

In order to realize the controllable loading of electromagnetic force in electromagnetic forming and improve the forming effect of tube, this paper puts forward an electromagnetic forming technology of tube based on double magnetic field converters. In this technology, two magnetic field converters are introduced between the tube and the driving coil, and the electromagnetic force is regulated by changing the geometric parameters and spacing of the magnetic field converters. Based on the specific 2024- aluminum alloy tube, the simulation research is carried out. The simulation data show that the change of the geometric structure and spacing of the two magnetic field converters can change the induced eddy current and realize the regulation of electromagnetic force. Compared with the traditional electromagnetic forming of tube, the uniform forming range D_r of electromagnetic forming of D_r based on double magnetic field converters is increased by 2.77 times. To sum up, the electromagnetic forming technology based on double magnetic field converters can effectively improve the forming uniformity of tube and promote the wide application of electromagnetic forming technology in industry.

keywords：Electromagnetic forming,magnetic field converter, electromagnetic force, uniformity

1. Introduction

Electromagnetic forming technology is the application of Lenz's law and Faraday's law of electromagnetic induction in engineering, which involves many professional fields such as materials science, electromagnetism and structural mechanics [1)2)]. The uniformity problem in electromagnetic forming technology generally exists in the electromagnetic forming process of workpieces. In the traditional electromagnetic bulging of tube, the driving coil is placed inside the tube to be expanded, and the electromagnetic force on the tube is mainly radial electromagnetic force. Because of the end effect of the driving coil, the radial electromagnetic force on the tube is unevenly distributed in the axial direction, which leads to the uneven radial deformation of the tube after forming. Scholars at home and abroad have launched a series of research work on this problem. Qiu Li et al. proposed a new type of coil structure "concave" to drive the coil to realize the electromagnetic forming of tube[3)]. By reducing the number of turns in the middle of the drive coil, the magnetic flux density and induced eddy current in the middle of the tube were greatly reduced, and the radial electromagnetic force on the middle of the tube was weakened, so that the radial electromagnetic force on the tube was distributed in a "concave" shape. After the method of "concave" drive coil loading the tube for electromagnetic bulging was put forward, Zhang et al. proposed the "convex" type. Using a single driving coil to process the workpiece has certain limitations. Cao et al. put forward an electromagnetic bulging method of tube with automatic feedback of electromagnetic force[4)], which introduces another driving coil outside the tube in the traditional electromagnetic bulging, and controls the electromagnetic force distribution of the tube through the regulation of the eddy current induced on the tube by the outer driving coil, so as to realize the axial uniform deformation of the tube. In addition, Ouyang et al. put forward a combined loading method with two coils[5)], which divided the driving coil into two sections, and improved the formability of the tube by changing the current waveform in the driving coil. Due to the diversity of driving coil loading, the multi-coil combined loading method is one of the hot research directions in the field of electromagnetic forming.

In recent years, with the continuous development of electromagnetic forming technology, the electromagnetic forming process is not limited to driving coils and workpieces, and some materials to assist electromagnetic forming are constantly emerging[6)7)]. Magnetic field converter is an important auxiliary tool in electromagnetic forming technology[8)9)10)11)]. Professor Manoj of Indian Institute of Science and Innovation studied the influence of materials of magnetic field converter on electromagnetic forming. The results show that the material and geometry of the magnetic field converter have significant influence on the forming

Corresponding author: CAO Cheng (e-mail: 1726298084@qq.com).

effect of the workpiece. In addition, Professor Rasoul of Amir kabir University of Technology introduced a stepped magnetic field converter structure, studied the influence of geometric parameters of this new magnetic field converter on electromagnetic force and forming effect, and designed the optimal geometric parameters of the magnetic field converter. Compared with the direct loading of the driving coil, the maximum magnetic pressure of the stepped magnetic field converter is increased by 21%[12]. On the basis of this research, Qiu et al. put forward a concave magnetic field transformer to solve the problem of tube forming uniformity.

Therefore, it can be seen that by introducing the magnetic field converter, the distribution of electromagnetic force in the electromagnetic forming system can be changed, and then the deformation process of the tube can be optimized and the forming uniformity of the tube can be improved[13)14)]. In this paper, the electromagnetic forming model of tube with double magnetic field converters is put forward. By introducing magnetic field converters at the upper and lower ends of the tube, the electromagnetic force at the ends of the tube is enhanced, so that the electromagnetic force on the tube is distributed in a concave shape as a whole, so as to regulate the distribution of electromagnetic force in the electromagnetic forming system and improve the uniformity of electromagnetic forming of tube. In order to explore the influence of double magnetic field converters on the electromagnetic forming effect of tube, a two-dimensional axisymmetric simulation model of electromagnetic forming of tube based on double magnetic field converters is built by Comsol simulation software, and the influence of the geometric structure of magnetic field converters on the forming effect in the electromagnetic forming system of tube based on double magnetic field converters is studied, and then the forming effects of traditional electromagnetic bulging of tube with single coil and electromagnetic bulging of tube based on double magnetic field converters are compared and analyzed. Finally, the feasibility of using double magnetic field converters to realize the bulging uniformity of tubes loaded with electromagnetic force is verified by simulation analysis.

2. Basic principle of electromagnetic forming of double magnetic field converter tube

Electromagnetic forming system generally includes power supply, driving coil, workpiece, free-wheeling circuit, switch, etc. The electromagnetic bulging system of tube is shown in Fig 1. First, charge the power supply. When the capacitor bank in the power supply gets enough electric energy, a large pulse current will be generated by closing the switch circuit. According to the law of electromagnetic induction, the change of magnetic field will induce eddy current in metal workpiece, and the interaction between induced eddy current and pulse current will produce a strong pulse electromagnetic force to deform the workpiece. The free-wheeling circuit in the circuit can reduce the temperature rise of the coil and improve the life of the coil.

The geometric configuration of a single coil fundamentally determines its magnetic field distribution. As coils are typically elongated or ring-shaped structures, the generated magnetic fields do not spread uniformly across space. Since electromagnetic force magnitude correlates directly with magnetic field strength, this creates a "strong at the center, weak at the ends" pattern that concentrates radial electromagnetic forces in the central region. The workpiece end effect arises from the inherent boundary characteristics of pipe components. When electromagnetic forces act on pipe ends, these ends aren't infinitely extended but have defined boundaries. At the ends, electromagnetic forces leak or weaken due to boundary effects, failing to form stable concentrated force fields like the central area. This imbalance ultimately intensifies the disparity where the core section experiences stronger forces while the ends endure weaker ones.In the electromagnetic forming process, it is difficult to reduce the distance between the coil and the workpiece by moving the coil due to the limitation of the forming system structure. By introducing the magnetic field transformer, the energy of the coil can be transferred to the workpiece through the magnetic field converter. The magnetic field converter is a ring with different heights of inner wall and outer wall, and there is a narrow gap in the ring structure[15)]. When the time-varying current passes through the magnetic field converter, most of the current will be concentrated on the surface of the conductor because of the skin effect, and the total current flowing through the inner and outer walls is equal in magnitude and opposite in direction. The inner wall and outer wall of the magnetic field converter are defined by the distance between the magnetic field converter and the driving coil, in which the side close to the driving coil is the inner wall and the side far from the driving coil is the outer wall. Fig. 2 is a schematic diagram of the three-dimensional structure of the magnetic field transformer. Because of the height difference between the inner and outer walls of the magnetic field converter, the current density of the outer wall and the inner wall of the magnetic field converter will be different.

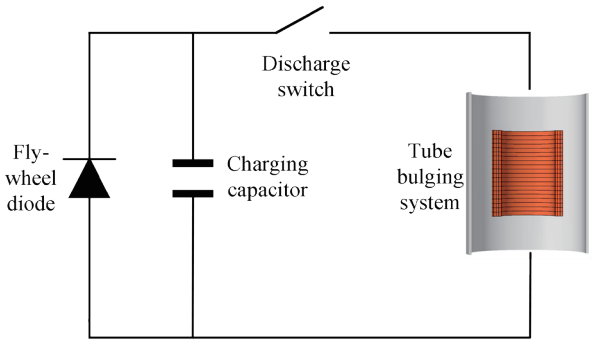

Fig.1 Schematic diagram of electromagnetic bulging system of tube

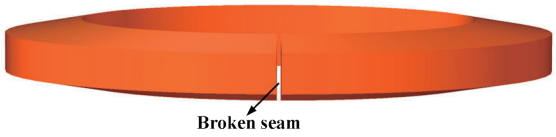

Fig.2 Three-dimensional schematic diagram of magnetic field converter

Therefore, the magnetic field converter can be used to change the distribution of induced eddy current and magnetic field in the forming workpiece, and then change the electromagnetic force distribution in the forming process of tube [16)17)].

Fig. 3 is the eddy current distribution diagram of the electromagnetic bulging system of tube[18)19)]. It can be seen from the eddy current directions in the tube, the driving coil and the magnetic field converter that the coil current is opposite to the inner wall current of the magnetic field converter, and the inner wall current flows from the inner wall to the outer wall through the gap of the magnetic field converter, so the total current of the inner and outer walls of the magnetic field converter is equal in magnitude and opposite in direction, and the outer wall current of the magnetic field converter is opposite to the eddy current induced by the tube.

Compared with the traditional electromagnetic forming uniformity of single-coil tube, the application advantage of double magnetic field converters in electromagnetic forming of tube proposed in this paper is to improve the magnetic field distribution and improve the forming uniformity of tube by introducing a reasonable magnetic field converters structure without changing the driving coil, as shown in Fig 4. The advantages of electromagnetic forming of tube with double magnetic field converters are that for driving coils, the coil does not need complicated winding process. On the basis of ordinary spiral coils, the electromagnetic forming uniformity of tube is improved by introducing double magnetic field converters.

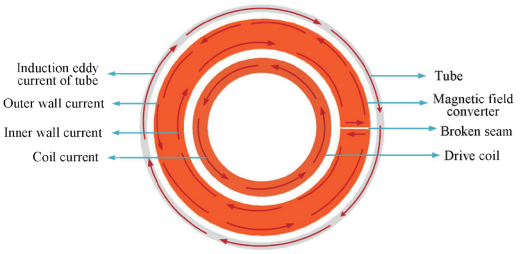

Fig.3 Eddy current distribution diagram of electromagnetic tube bulging system

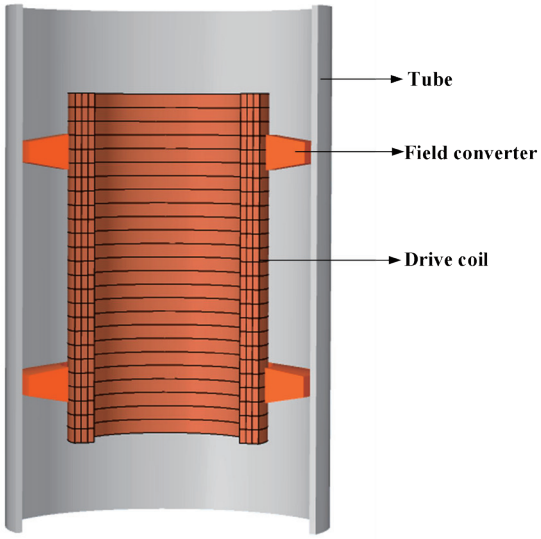

Fig.4 Three-dimensional schematic diagram of tube bulging of two field converters

In different applications, the control of magnetic field and electromagnetic force can be realized only by changing the structure of the magnetic field transformers. For driving coils with specific structures and sizes, the application scope and application occasions are wider, which is more conducive to saving the manufacturing cost of driving coils. In addition, due to the introduction of double magnetic field converters in the electromagnetic forming system, for tube, the electromagnetic force at both ends is enhanced by the end magnetic field converter to overcome the end effect, which is beneficial to improve the electromagnetic forming uniformity of tube and the quality of industrial products is higher.

3. Numerical simulation model

In this paper, COMSOL multi-physical finite element simulation software is used to establish a two-dimensional axisymmetric model of electromagnetic bulging of tube based on double magnetic field converters[18)19)].

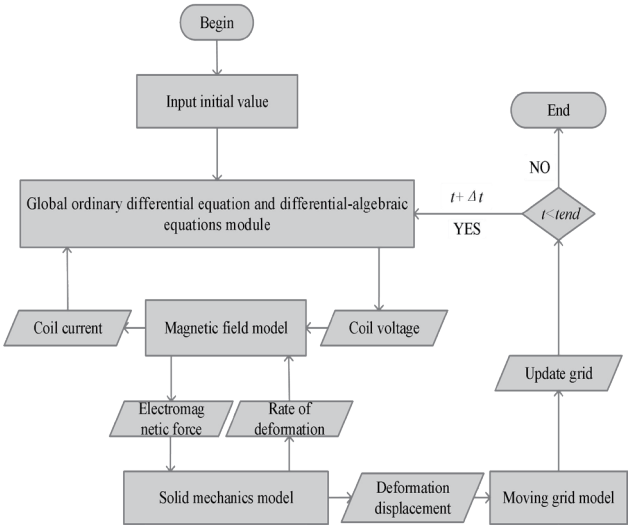

Fig.5 Simulation flow chart of electromagnetic forming of tube

The simulation flow chart is shown in Fig 5, where t represents the current time, Δt represents the time step and t_{end} is the end time.

The simulation model mainly includes four modules: global ordinary differential equation and differential-algebraic equations module, electromagnetic field module, solid mechanics module and "moving grid" module [20)21)].

1.Global ordinary differential equation and differential-algebraic equations module:

This module is used to solve the coil current. In this paper, the electromagnetic bulging circuit model of tube with free-wheeling circuit is adopted, as shown in Fig 6 [22)23)24)]. According to Kirchhoff's law, the following circuit equations can be obtained:

$$\begin{cases} \boldsymbol{I}_{coil}(R_c+R_1)+(L_c+L_1)\dfrac{d\boldsymbol{I}_{coil}}{dt}+M_{cw}\dfrac{d\boldsymbol{I}_w}{dt}=\boldsymbol{U}_c \\ R_w\boldsymbol{I}_w+L_w\dfrac{d\boldsymbol{I}_{coil}}{dt}=0 \\ U_0-\dfrac{1}{C}\int_0^t \boldsymbol{I}_c dt=\boldsymbol{U}_c \\ \boldsymbol{I}_c+\boldsymbol{I}_d-\boldsymbol{I}_{coil}=0 \end{cases} \quad (1)$$

The free-wheeling circuit equation is:

$$\begin{cases} \boldsymbol{I}_d=0(\boldsymbol{U}_c\geq 0) \\ \boldsymbol{I}_d=\dfrac{\boldsymbol{U}_c}{R_d}(\boldsymbol{U}_c<0) \end{cases} \quad (2)$$

$\boldsymbol{U}_C$ is the voltage across the capacitor. U_0 is the initial voltage of the capacitor, $\boldsymbol{I}_{coil}$ is the drive coil current. $\boldsymbol{I}_c$ is the discharge loop current. $\boldsymbol{I}_W$ is the induced eddy current of the tube. $\boldsymbol{I}_d$ is the current of the freewheeling circuit. R_c is the resistance of the drive coil. R_1 is the discharge circuit resistance. R_d is the free-wheeling circuit resistance. R_w is the resistance of the tube. L_1 is the inductance of the discharge circuit. L_c is the inductance of the drive coil. L_W is the tube inductance. M_{cw} is the coupling coefficient between the tube and the coil.

Magnetic field transformer is introduced as an electromagnetic forming aid, and its circuit is shown in Fig 7. The magnetic field converter and the driving coil have a coupling relationship, and then the energy generated by the driving coil is transferred to the tube through the magnetic field converter, ignoring the coupling between the tube and the driving coil, and the circuit equation can be changed to:

$$\begin{cases} \boldsymbol{I}_{coil}(R_c+R_1)+(L_c+L_1)\dfrac{d\boldsymbol{I}_{coil}}{dt}+M_{cf}\dfrac{d\boldsymbol{I}_f}{dt}=\boldsymbol{U}_c \\ R_w\boldsymbol{I}_w+L_w\dfrac{d\boldsymbol{I}_{coil}}{dt}=0 \\ U_0-\dfrac{1}{C}\int_0^t \boldsymbol{I}_c dt=\boldsymbol{U}_c \\ \boldsymbol{I}_c+\boldsymbol{I}_d-\boldsymbol{I}_{coil}=0 \\ R_f\boldsymbol{I}_f+L_f\dfrac{d\boldsymbol{I}_f}{dt}=0 \end{cases} \quad (3)$$

The free-wheeling circuit equation remains unchanged. I_f is the induced current of the magnetic field converter. R_f is the resistance of the magnetic field converter. L_f is the inductance of the magnetic field converter. M_{cf} is the mutual inductance between the magnetic field converter and the coil. M_{fw} is the mutual inductance coefficient between the magnetic field converter and the tube. Table1 shows the relevant circuit parameters of tube bulging system. M_{cw} is the coupling coefficient between the tube and the coil, which is weaker than that between the coil and the magnetic field converter and between the magnetic field converter and the tube, and is usually ignored.

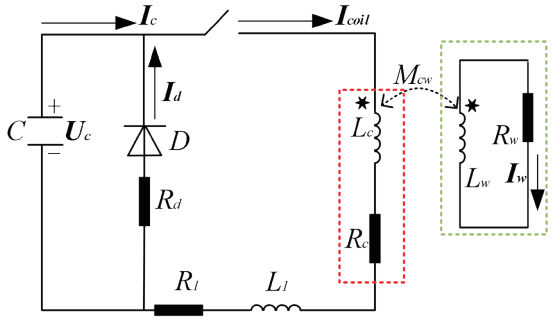

Fig.6 Equivalent circuit diagram of electromagnetic forming

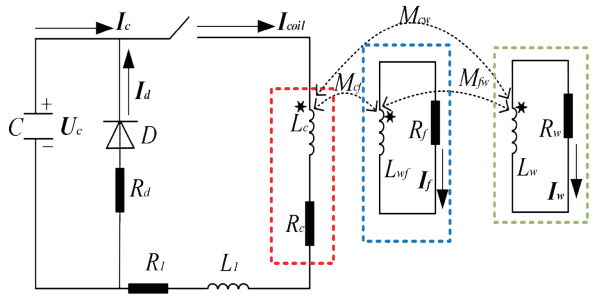

Fig.7 Equivalent circuit diagram of electromagnetic bulging based on magnetic field converter

2.Electromagnetic field module:

Which is used for obtaining the distribution of magnetic field and electromagnetic force and transmitting the obtained electromagnetic force to the solid mechanics module. The induced eddy current in the workpiece is mainly annular component, and the magnetic field can be expressed by Maxwell equation:

$$\begin{cases} \nabla \times \boldsymbol{H} = \boldsymbol{J} \\ \nabla \times \boldsymbol{E}_\varphi = -\dfrac{\partial \boldsymbol{B}_z}{\partial t} + \nabla \times (\boldsymbol{v}_z \times \boldsymbol{B}_r) \\ \nabla \bullet \boldsymbol{B} = 0 \\ \boldsymbol{J}_\varphi = \dfrac{\boldsymbol{I}_c}{S} = \gamma \boldsymbol{E}_\varphi \end{cases} \tag{4}$$

$\boldsymbol{E}$ is the electric field strength,$\boldsymbol{B}$ is the magnetic flux density,$\boldsymbol{v}$ is the pipe deformation speed.$\boldsymbol{J}$ is the density of induced eddy current. γ is the tube conductivity.The subscripts r, φ and z represent the radial, circumferential and axial components of the vector respectively.

$$\begin{cases} \boldsymbol{F}_r = \boldsymbol{J}_\varphi \times \boldsymbol{B}_z \\ \boldsymbol{F}_z = \boldsymbol{J}_\varphi \times \boldsymbol{B}_r \end{cases} \tag{5}$$

$\boldsymbol{F_r}$ is the radial electromagnetic force on the pipe fitting.$\boldsymbol{F_z}$ is the axial electromagnetic force on the tube, and $\boldsymbol{J_\varphi}$ is the circumferential induced eddy current density. The electromagnetic force on the tube is determined by the tube magnetic flux density and its own induced eddy current. For the electromagnetic bulging system of the tube, the magnetic field around the tube is mainly distributed in the axial direction, so the forming process of the tube is mainly driven by the radial electromagnetic force, and the axial electromagnetic force can usually be ignored.

3.Solid mechanics module:

This model is used to model the plastic deformation of the workpiece. The displacement equation of double magnetic field converter is:

$$\rho \frac{\partial^2 \boldsymbol{u}}{\partial t^2} - \nabla \bullet \boldsymbol{\sigma} = \boldsymbol{F_m} \tag{6}$$

σ is the stress tensor, $\boldsymbol{F_m}$ is the electromagnetic force density, ρ is the tube density, and $\boldsymbol{u}$ is the displacement. In this paper, the 2024- aluminum alloy tube is simulated, and the deformation behavior of the tube under the high-speed collision of double magnetic field converters will affect its material constitutive model.2024 aluminum alloy, renowned for its low density, crack resistance, and fatigue durability, serves as the primary material for aircraft skin components and other thin-walled complex structures. However, traditional cold stamping methods used to manufacture 2024 aluminum alloy aircraft skins often result in issues like wrinkling, cracking, and insufficient precision, posing significant technical challenges for high-performance manufacturing of these critical components.However, the electrical conductivity of 2024 aluminum alloy is only $1.87e^7$, which means a higher discharge voltage is required during electromagnetic forming to achieve pipe bulging, and the end effect becomes more pronounced. Compared with other high-conductivity aluminum alloys, introducing a magnetic field converter to enhance the magnetic field around the 2024 alloy and its induced eddy currents is more meaningful than in other types of aluminum alloys. Cowper-Symonds material constitutive model is adopted to describe the plastic deformation process of the tube under the collision of double magnetic field converters, and its constitutive equation is[25]:

$$[1+(\frac{\varepsilon_{pe}}{G})^m]\sigma_{ys} = \sigma \tag{7}$$

In the equation, $\boldsymbol{\sigma_{ys}}$ is the initial yield stress of tube, m is the strain rate hardening parameter, $\boldsymbol{\varepsilon_{pe}}$ is the plastic strain rate, and G is the viscosity density. In this paper, G=6500 and m=0.25[26].

4."Moving grid" module:

It is used to update the air grid around the tube fitting, improve the simulation accuracy and avoid grid distortion during bulging [27)28)].

Table1 Circuit parameters

Symbol	Describe	Numerical value
C	Power supply capacitance	320μF
L_1	Loop inductance	12μH
R_1	Loop resistance	0.025Ω
R_d	Flywheel resistance	0.25Ω
U_0	Discharge voltage	7kV

4. Simulation results and analysis

Based on the above external circuit and workpiece parameters, the simulation model is built. The magnitude and distribution of electromagnetic force on the tube is closely related to the structural parameters of the double magnetic field converters. In this paper, the tube bulging is qualitatively and quantitatively analyzed from two aspects: radial electromagnetic force density and radial displacement of the tube. The main material parameters of each component of the tube bulging system in the simulation model are shown in Table 2. The geometric structure of electromagnetic bulging model of single-coil tube is shown in Fig 8a, and that of double-magnetic field converters tube is shown in Fig 8b. Under the condition of keeping the position, structure and material properties of tube and coils unchanged, the effects of the distance Ha of magnetic field converter and the height Hb of the outer wall of magnetic field transformer on the forming uniformity of tube are studied respectively. The distance between the magnetic field converters and the coil is 2.0 mm, and the distance between the magnetic field converters and the tube is 2.0 mm.. The thickness of 2024- aluminum alloy tube is 2.0 mm.

Table2 Material parameters in simulation model

Package	Parameter	Symbol	Numerical value
Tube	Density/(kg·m^{-3})	ρ_w	2730
	Electrical conductivity/(S·m)	σ_w	1.87e^7
	Poisson's ratio	γ_w	0.3
	Young's modulus/GPa	E_w	73
Magnetic field converter	Electrical conductivity/(S·m)	σ_f	5.998e^7
	Density/(kg·m^{-3})	ρ_f	8700
Drive coil	Density/（kg·m^{-3}）	ρ_c	8700
	Electrical conductivity/(S·m)	σ_c	5.998e^7

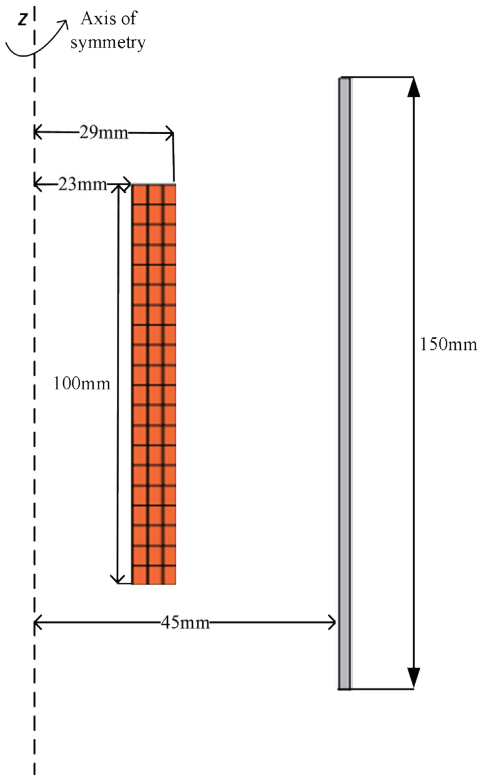

(a) No magnetic field converter

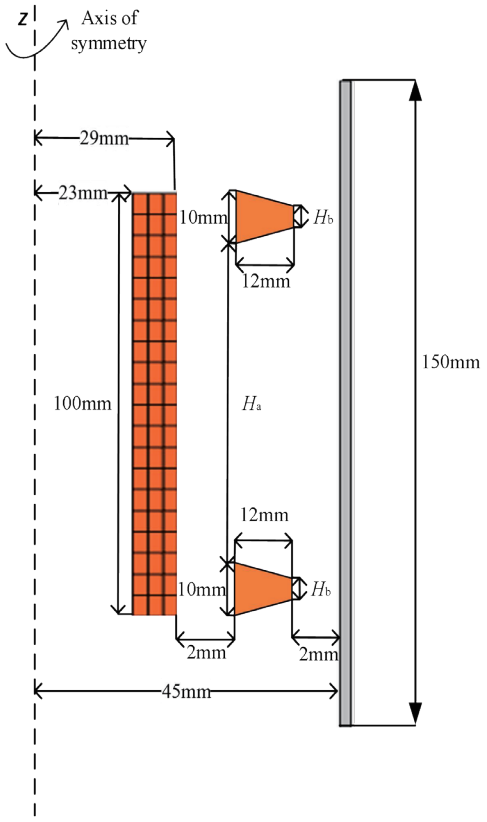

(b) Two magnetic field converter

Fig.8 Numerical simulation structure parameter diagram

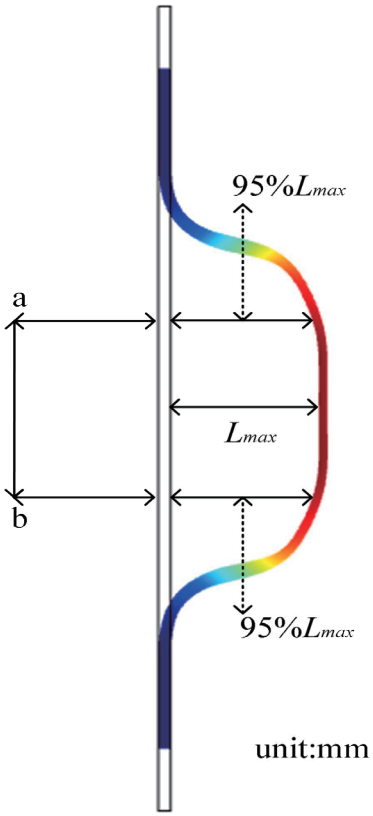

Fig.9 Parameter definition diagram

4.1 Influence of geometric parameter of magnetic field converter on tube for effect

In order to evaluate the uniformity of electromagnetic bulging of tube and realize quantitative analysis of uniformity, this paper defines the uniformity criterion of electromagnetic forming of tube with two magnetic field converters. L_{max} is the maximum axial displacement distance of the tube fitting, 95%L_{max} is the maximum displacement distance of 95%, points A and B are on the tube, and the axial length between points A and B is the tube uniformity D_r. As shown in fig. 9.

4.1.1 magnetic field converters spacings:H_a

The influence of different magnetic field converters spacings on the tube bulging uniformity was analyzed. The geometric dimensions of the two magnetic field transformers were kept unchanged, and nine groups of different magnetic field converter spacings were selected, ranging from 35.8 mm to 42.2 mm, with a step size of 0.8 mm. The simulation results show that with the increase of H_a the energy coupled to the end magnetic collector decreases gradually, so the peak value of the radial electromagnetic force density of the tube in Fig 10a decreases from 3.72×10^9N·m^{-3} to 2.98×10^9 N m^{-3}. After the introduction of the double magnetic field converter, the peak value of the electromagnetic force of the tube is at the two ends of the tube, and the positions where the two radial electromagnetic force density peaks appear are farther away from the axial center of the tube, from 44.5 mm and 105.5 mm to 38 mm and 112 mm,respectively.The radial electromagnetic force in the middle of the tube is basically unchanged, and the radial electromagnetic force on the tube is distributed in a concave shape along the axial direction as a whole. As shown in Fig 10b, the influence of H_a on the forming effect of tube. With the increase of H_a, the peak value of radial electromagnetic force density of tube gradually moves away from the center of tube, and the bulging profile of tube transits from concave to convex. The forming uniformity is the best when the bulging profile of tube transits from concave to convex, which is 38.2 mm in this calculation example.

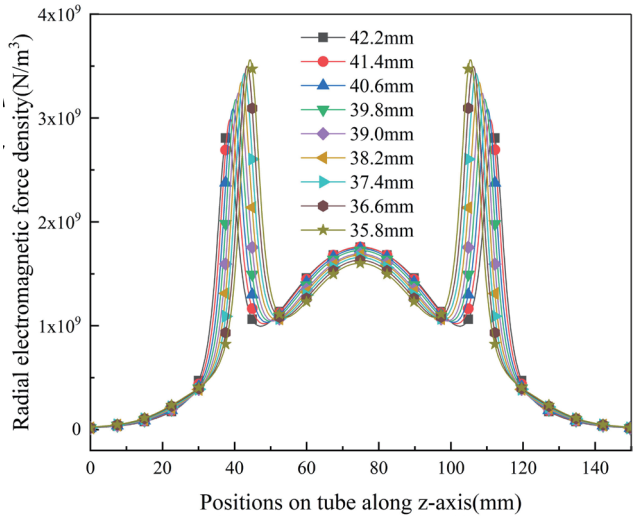

(a) Radial electromagnetic force density

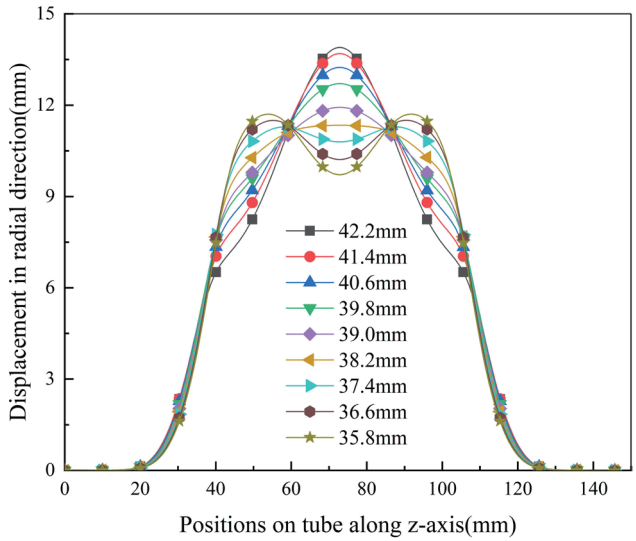

(b) Displacement in radial direction

Fig.10 Influence of magnetic field converter spacing on the electromagnetic tube bulging

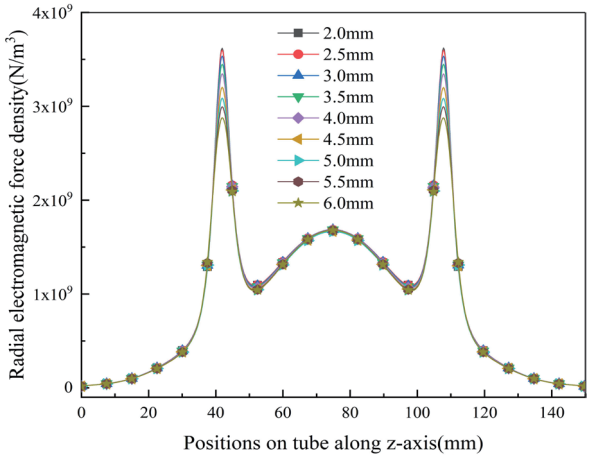

(a)Radial electromagnetic force density

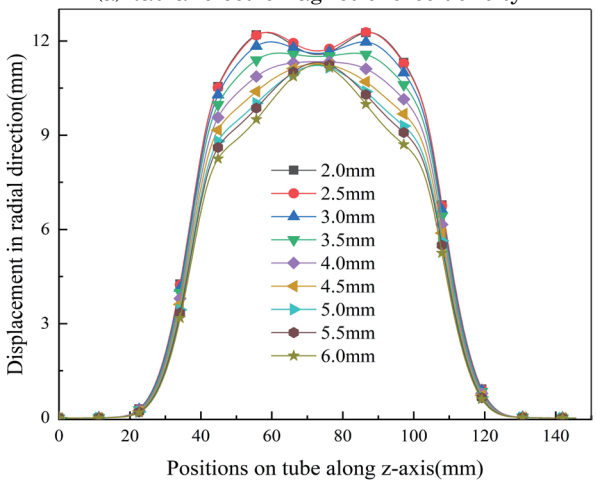

(b) Displacement in radial direction

Fig.11 Influence of height of outer wall of magnetic field transformer on the electromagnetic tube bulging

4.1.2 Outer wall heights of magnetic field converters: H_b

When analyzing the influence characteristics of different outer wall heights of magnetic field converters on tube bulging uniformity, the distance between magnetic field converters is kept constant, always 38.2 mm;Take different heights H_b of the outer wall of the magnetic field converters, ranging from 2 mm to 6 mm, with a step size of 0.5 mm, and the influence of H_b on the radial electromagnetic force density is shown in Fig 11a. With the increase of H_b, the electromagnetic force density on the tube end gradually decreased from 3.75×10^9N·m^{-3} to 2.95×10^9 N·m^{-3}. Because the induced current density of the inner wall of the magnetic field transformer remains unchanged, but the induced current density of the outer wall decreases due to the increase of the area of the outer wall, the electromagnetic force density on the end of the tube decreases and the length of the peak axial span increases slightly, and the radial electromagnetic force density in the middle of the tube will not change basically because of the increase of H_b, and the radial electromagnetic force density of the tube is still concave as a whole. The influence of H_b on the forming effect of tube is shown in Fig 11b. With the increase of H_b, the maximum bulging position of the tube gradually transits from both ends to the middle, and the forming profile of the tube gradually transits from "concave" to "convex". When H_b is 4 mm, the overall forming profile of the tube is the smoothest.

4.2 Comparative analysis of forming effect of electromagnetic forming method for tube

In order to reflect the improvement effect of double magnetic field converters on the tube bulging uniformity, this paper uses the traditional single coil tube bulging method and double magnetic field converters tube bulging method to process the same tube respectively, analyzes and compares the distribution of electromagnetic force density under the two methods, and compares the tube forming uniformity. The maximum bulging amount of tube under the two forming methods is 11.5 mm, the voltage of electromagnetic bulging of tube without magnetic field converter is 6.45 kV, and the voltage of electromagnetic bulging of tube with double magnetic field converters is 7 kV.

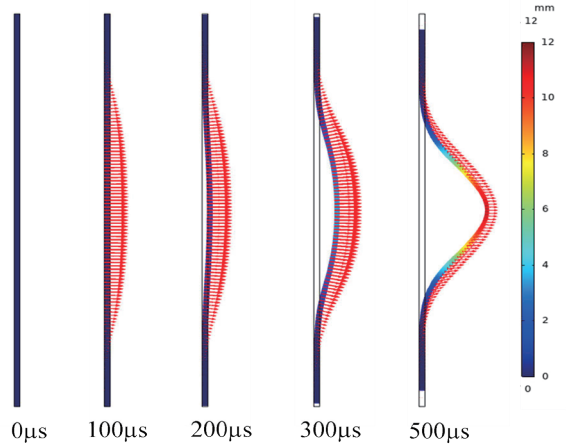

(a) Tube bulging of traditional single coil

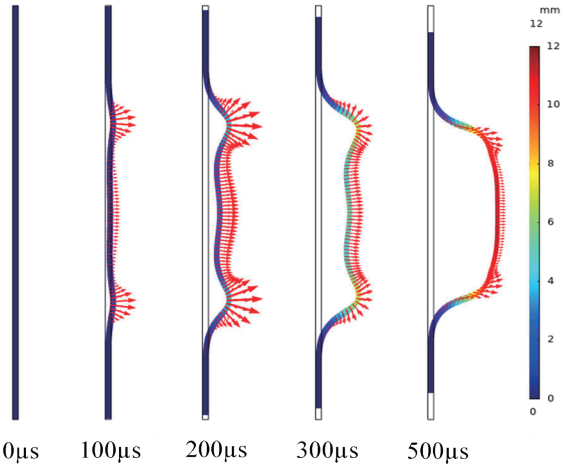

(b) Tube bulging of double magnetic field converter

Fig.12 Dynamic distribution law of electromagnetic force under two bulging modes

Fig. 12 shows the electromagnetic force density distribution on the surface of the tube at different time points under two bulging methods. It can be seen that in the tube bulging without magnetic field converters, the electromagnetic force is mainly concentrated in the middle of the tube, and the tube bulging begins at 100 μs and basically ends at 500 μs, and the electromagnetic force and deformation are mainly concentrated in the middle. In the tube bulging of double magnetic field converters, before 200 μs, the electromagnetic force is mainly concentrated at the end of the tube, and the end of the tube is deformed first at 100 s. After 200 μs, the electromagnetic force in the middle of the tube began to increase, and the middle of the tube began to deform under the electromagnetic force and the "pull" of the end. After 300 μs, the middle part of the tube expands further under the action of electromagnetic force, and the bulging of the 500 μs tube basically ends.

The radial electromagnetic force density distribution of tube under two loading modes is shown in Fig 13a. The radial electromagnetic force density in the axial middle part of the tube is the largest in the electromagnetic bulging of the tube without magnetic field converter based on single coil. However, when adopting the tube bulging structure of double magnetic field converter, the electromagnetic force density at the end of the tube is enhanced, and the electromagnetic force density is no longer concentrated in the middle of the tube, and the radial electromagnetic force density is generally concave. The radial displacement of tube is shown in Fig 13b. In this paper, the bulging area of tube with bulging amount greater than 3 mm is defined as the effective bulging range L_z. Due to the introduction of two end magnetic field converters, the electromagnetic force at the end of the tube is enhanced, so the expansion range of the tube is larger than that of the tube without magnetic field transformer, and the L_z is 72 mm and 39 mm respectively under the two expansion methods. In the electromagnetic bulging system of tube without magnetic field converter, the radial displacement of tube is concentrated in the axial center of tube, and the bulging amount in the middle of tube is obviously larger than that in other areas. However, in the electromagnetic bulging system of tube based on double magnetic field converters, the radial electromagnetic force density with concave distribution increases the bulging amount at the end of tube, which drives the axial middle bulging through the end, so the bulging is more flat and uniform.

Fig. 14 is a three-dimensional outline diagram of tube bulging, in order to compare the bulging uniformity of tube under two bulging methods. The D_r of traditional tube bulging with single coil is 11 mm, and that of tube bulging with three magnetic collectors is 41.5 mm. By comparison, the uniformity of tube bulging with double magnetic field converters is improved by 2.77 times.

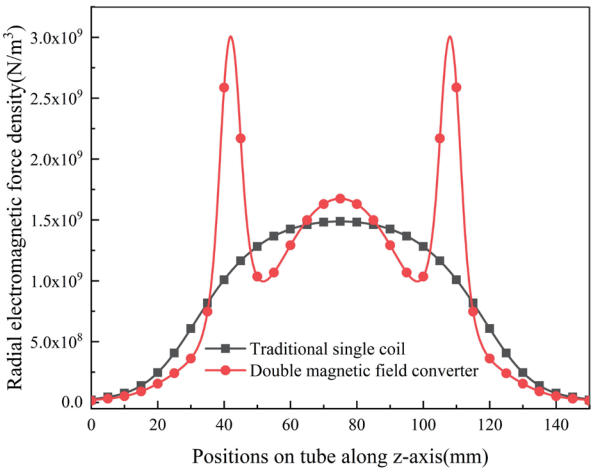

(a) Radial electromagnetic force density

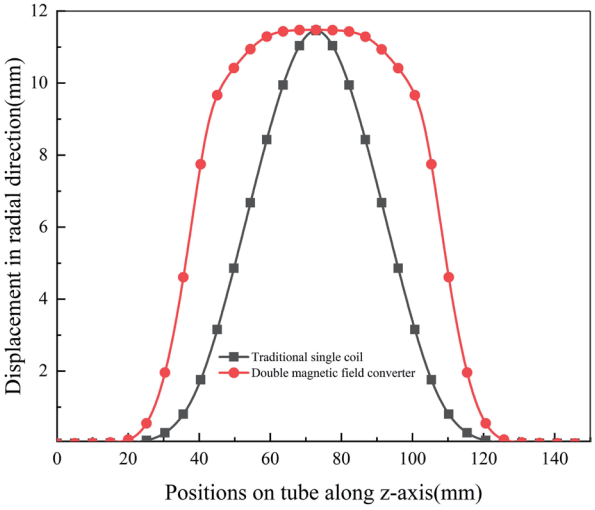

(b) Radial displacement

Fig.13 Radial electromagnetic force density and radial displacement under two bulging modes

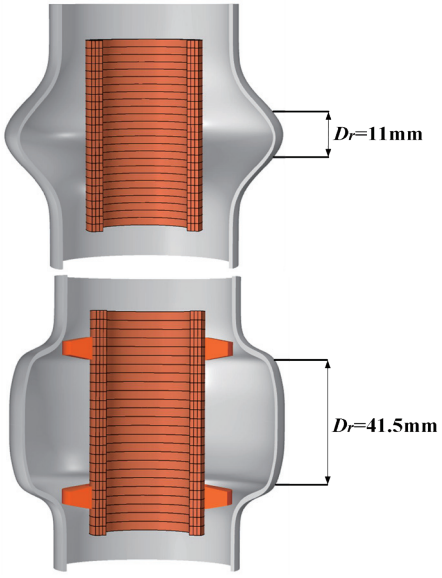

Fig.14 Three-dimensional forming effect diagram of tube with two forming methods

5. Conclusion

Aiming at the technical defects existing in the traditional electromagnetic forming technology of tube, this paper puts forward an electromagnetic forming technology of tube based on double magnetic field converters to solve the problems of difficult regulation of electromagnetic force and poor bulging uniformity of tube. The research proves that the flexible regulation of electromagnetic force in the forming system can be realized by changing the spacing and geometric structure of the magnetic field converters, and the simulation results prove that the deformation behavior of the tube is more conducive to the uniform deformation of the tube after introducing the double magnetic field converters. In the simulation model example of this paper, the electromagnetic forming uniformity of the tube is the best when the spacing of the magnetic field converters is 38.2 mm and the outer wall of the magnetic field transformers is 4 mm, and the uniform forming range D_r is 41.5mm, which is 2.77 times higher than that of the traditional electromagnetic forming of the tube.

References

1) V. S. Balanethiram, S. D. Glenn: *Scripta Metallurgica Materialia,* **27,** 12 (1992).
2) P. J. Ferreira, J. B. Sande, and M. A. Fortes: *Metallurgical and Materials Transactions,* **35,** 3091 (2004).
3) Q. Li,Y. Yijie, N. Xiaopeng: *Journal of Electrotechnical Technology,* **34**, 212 (2019).
4) Z. Wang, O. Shaowei: *Journal of Materials Processing Technology,* **313**, 1 (2023).
5) O. Shaowei: *The International Journal of Advanced Manufacturing Technology,* **114**, 1533 (2021).
6) L. Xin, W. Litong, and L Guishu： *Transactions of China Electrotechnical Society,* **35**,1 (2020).
7) M.Kamal:. *Journal of Manufacturing Science and Engineering,* **129**, 369 (2007).
8) X. Shijie, M. Jianhua, and C. Xiaohui: *New technology and new process* ,**4,**54 (2012).
9) Q. Li, D. Kui, and X. Qi : *IEEE Trans,* **99**, 1 (2020)
10) Q. Li, Y. Ningxuan, and A. S. Ahmed: *IEEE Trans*, **81**, 6166 (2020).
11) S. Golowin, M. Kamal, and J. Shang: *Journal of Materials Engineering and Performance,* **16**,455 (2007).
12) R. Chaharmiri, A. F. Arezoodar: *Journal of Manufacturing Science and Engineering,* **139**,1 (2017).
13) X. Qi, L. Qingshan, and L. Zhe: *Journal of Electrotechnical Technology,* **38**, 285 (2023).
14) L. Chunfeng, Y. Haiping: *Journal of Plastic Engineering,* **5**,1 (2005).
15) K. R. Ashish, K. Ramesh, and D. K. Sachin: *Journal of Mechanical Science and Technology,***33**,5407 (2019).
16) R. K. Mohammed, S. Archana: *Arabian Journal for Science and Engineering,* **44**,1129 (2019).
17) A. K. Rajak, R. Kumar, and H. Basumatary: *International Journal of Precision Engineering and Manufacturing,* **19**, 453 (2018).
18) Q. Li, W. Weiye, and A. S. Ahmed: *IEEE Trans,* **9,**70014 (2021).
19) Y. Ziqin, L. Lie, and C. Yang: *International Journal of Advanced Manufacturing Technology,***120**, 1747 (2022).
20) Q. Li, T. Xi, and W. Weiye: *Precision Forming Engineering,* **14**,17 (2022).
21) Q. Li, L. Yantao , and S. Pan: *Journal of Electrotechnical Technology,* **34**,2247(2019).
22) Q. Li,Y. Yijie, and Y. Yuqi:*International Journal of Applied Electromagnetics and Mechanics,* **57**,29 (2018)
23) Q. Li, Y. Xinsen, and C. Peng: *Journal of Electrotechnical Technology,* **34**, 2855 (2019).
24) O. Shaowei, L. Xiaoxiang, and L. Changxing: *Journal of Manufacturing Processes,* **49**, 102 (2020).
25) Q. Li, W. Chenglin: *Smart Power,* **49**, 97 (2021).
26) L. Xianlong, H. Liang, and L. Jianjun: *The International Journal of Advanced Manufacturing Technology,* **104**, 411 (2019).
27) Z. Wang, W. Yudong, and L. Yantao: *Journal of Electrotechnical Technology,* **36**, 2904 (2021).
28) Q. Li ,L. Yutian ,and A. S. Ahmed:*IEEE Trans,* **9**, 63550(2021).

Received Aug.24,2025;Revised Oct.06,2025;Accepted Dec.12,2025

Editorial Committee Members・Paper Committee Members

Notice for Photocopying

編集委員・論文委員

複写をされる方へ

Journal of the Magnetics Society of Japan

Vol. 50 No. 2 (通巻第344号) 2026年3月1日発行

Vol. 50 No. 2 Published Mar. 1, 2026
by the Magnetics Society of Japan
Tokyo YWCA building Rm207, 1–8–11 Kanda surugadai, Chiyoda-ku, Tokyo 101–0062
Tel. +81–3–5281–0106　Fax. +81–3–5281–0107

Printed by JPC Co., Ltd.
Sports Plaza building 401, 2–4–3, Shinkamata Ota-ku, Tokyo 144–0054
Advertising agency: Kagaku Gijutsu-sha

発行：(公社)日本磁気学会　101–0062　東京都千代田区神田駿河台 1–8–11　東京YWCA会館 207 号室
製作：ジェイピーシー　144–0054　東京都大田区新蒲田 2–4–3　スポーツプラザビル401　Tel.（03）6715–7915
広告取扱い：科学技術社　111–0052　東京都台東区柳橋 2–10–8　武田ビル 4F　Tel.（03）5809–1132